1 # Assessing the Sensitivity of Aerosol Mass Budget and

2 # Effective Radiative Forcing to Horizontal Grid Spacing in

3 # E3SMv1 Using A Regional Refinement Approach

4 Jianfeng Li[1, *], Kai Zhang[1, *], Taufiq Hassan[1], Shixuan Zhang[1], Po-Lun Ma[1], Balwinder Singh[1],
5 Qiyang Yan[1, a], Huilin Huang[1]

6 [1]Atmospheric Sciences and Global Change Division, Pacific Northwest National Laboratory,
7 Richland, Washington, US

8 [a]now at KLA Corporation, US

10 * Correspondence to Jianfeng Li (jianfeng.li@pnnl.gov) and Kai Zhang (Kai.Zhang@pnnl.gov)

Abstract

Atmospheric aerosols have important impacts on air quality and the Earth-atmospheric energy balance. However, as computing power is limited, Earth system models generally use coarse spatial grids and parameterize finer-scale atmospheric processes. These parameterizations and the simulation of atmospheric aerosols are often sensitive to model horizontal resolutions. Understanding the sensitivities is necessary for the development of Earth system models at higher resolutions with the deployment of more powerful supercomputers. Using the Energy Exascale Earth System Model (E3SM) version 1, this study investigates the impact of horizontal grid spacing on the simulated aerosol mass budget, aerosol-cloud interactions, and the effective radiative forcing of anthropogenic aerosols (ERF_{aer}) over the contiguous United States. We examine the resolution sensitivity by comparing the nudged simulation results for 2016 from the low-resolution model (LR) and the regional refinement model (RRM).

As expected, the simulated emissions of natural dust, sea salt, and marine organic matter are substantially higher in the RRM than in the LR. In addition, RRM simulates stronger aqueous-phase production of sulfate through the enhanced oxidation of sulfur dioxide by hydrogen peroxide due to increased cloud liquid water content. In contrast, the gas-phase chemical production of sulfate is slightly suppressed. The RRM resolves more large-scale precipitation and produces less convective precipitation than the LR, leading to increased (decreased) aerosol wet scavenging by large-scale (convective) precipitation.

Regarding aerosol effects on clouds, RRM produces larger temporal variabilities of large-scale liquid cloud fractions than LR, resulting in increased microphysical cloud processing of aerosols (more interstitial aerosols are converted to cloud-borne aerosols via aerosol activation) in RRM. Water vapor condensation is also enhanced in RRM compared to LR. Consequently, the RRM simulation produces more cloud droplets, a larger cloud droplet radius, a higher liquid water path, and a larger cloud optical depth than the LR simulation. A comparison of the present-day and pre-industrial simulations indicates

36   that, for this contiguous United States domain, the higher resolution increases ERF_{aer} at the top of the

37   model by about 12%, which is mainly attributed to the strengthened indirect effect associated with

38   aerosol-cloud interactions.

1 Introduction

Atmospheric aerosols have played essential roles in the deterioration of air quality in recent decades, especially in rapidly developing countries (Li et al., 2019; Lim et al., 2020; Xiao et al., 2021). Besides directly degrading atmospheric visibility and with substantial impacts on human health (Apte et al., 2015; Wang et al., 2019), aerosols are also involved in the formation of other major atmospheric pollutants, such as ozone and nitrogen oxides (Perring et al., 2013; Pusede et al., 2015). In addition, atmospheric aerosols from natural and anthropogenic sources considerably affect the radiation balance of the Earth system. The present-day (PD) (the year 2014) anthropogenic aerosol effective radiative forcing (ERF_{aer}) relative to the pre-industrial (PI) period (the year 1850) is estimated to range from -0.63 to -1.37 W m^{-2} according to 17 Earth system models (ESMs) participating the Coupled Model Intercomparison Project Phase 6 (CMIP6) (Smith et al., 2020). Aerosols can modulate the earth-atmospheric energy balance via several pathways. Firstly, they directly scatter and absorb shortwave and longwave radiation. Secondly, they are involved in cloud formation by acting as cloud condensation nuclei (CCN) and ice nuclei, thus influencing cloud radiative forcing. Thirdly, light-absorbing aerosols depositing on snow and ice ~~surface~~surfaces can change the snow and ice melting by absorbing more solar radiation, leading to changes in surface albedo and energy budgets (Qian et al., 2015). Aerosols can also indirectly affect the global energy budget by influencing the ocean biogeochemistry and terrestrial ecosystems (Hamilton et al., 2022; Jickells et al., 2005; Mahowald et al., 2017).

Accurate simulation of atmospheric aerosols in ESMs is challenging due to complex physical and chemical processes (e.g., emissions, nucleation, coagulation, condensation, dry deposition, wet scavenging and resuspension, droplet activation, gas- and aqueous-phase chemistry, and radiation) and our incomplete understanding of these processes. Substantial parameterizations are designed to represent the aerosol lifecycle and its interactions with clouds and radiation in the Energy Exascale Earth System Model (E3SM) (Burrows et al., 2022; Wang et al., 2020) — a state-of-the-science ESM sponsored by the

63   United States (US) Department of Energy (DOE) for scientific and energy mission applications (Golaz et

64   al., 2022; Golaz et al., 2019). However, these parameterizations are primarily developed and evaluated at

65   ESM scales, and their performance at higher resolution is generally unclear. As the computing power

66   continues to increase, future ESMs are expected to run at much higher resolutions (Caldwell et al., 2021;

67   Dueben et al., 2020; Heinzeller et al., 2016). Therefore, it is crucial to understand the fidelity of these

68   aerosol parameterizations and how the simulated aerosol lifecycle and aerosol effects on cloud and

69   radiation will change as model resolution increases. These efforts are critical for parameter tuning and

70   model development at high resolutions (Caldwell et al., 2019; Ma et al., 2014; Ma et al., 2015).

71   Caldwell et al. (2019) and Feng et al. (2022) investigated the impacts of model horizontal resolutions

72   on some aspects of the aerosol lifecycle in E3SM. However, both studies were based on simulations with

73   global uniform resolutions, which will be computationally expensive when the model resolution increases

74   further to convection-permitting. To reduce the computational cost and maintain high-resolution features,

75   variable-resolution techniques with high-resolution grids in the region of interest transitioning to low-

76   resolution meshes in others have been widely applied in ESMs (Harris et al., 2016; Schwartz, 2019;

77   Zarzycki et al., 2014). Tang et al. (2019) developed a regional refinement model (RRM) configuration for

78   E3SM version 1 (E3SMv1) with high-resolution meshes (~25 km) over the contiguous US (CONUS) and

79   low-resolution meshes (~100 km) in other areas. They found that RRM highly resembles the uniform

80   high-resolution simulation in the refined region, indicating that RRM can be an effective and

81   computationally efficient configuration for high-resolution model development.

82   This study investigates the impact of horizontal grid spacing on aerosol mass budget, aerosol-cloud

83   interactions, and ERF_{aer} over the CONUS in 2016 using the RRM configuration. We compare E3SMv1

84   simulations with a global uniform grid spacing of ~100 km (hereafter referred to as the low-resolution

85   (LR) simulations) to the RRM simulations using the same configuration as Tang et al. (2019) with higher

86   resolution (~25km) meshes over CONUS. Our findings provide insights into aerosol parameterization

87   development and their dependence on model horizontal resolution. The paper is organized as follows.

88 Section 2 describes the E3SMv1 model and the simulation configurations. Section 3 discusses the impacts

89 of increasing resolution on 1) the natural aerosol sources, 2) the aerosol wet scavenging, 3) the aerosol

90 chemical production, 4) the aerosol-cloud interactions, and 5) ERF_{aer}, where apparent discrepancies are

91 found between the LR and RRM simulations. Finally, the study is summarized in Section 4.

2 Model setup

2.1 E3SMv1 model description

94 Aerosol processes are primarily represented in the E3SM Atmosphere Model version 1 (EAMv1)

95 (Rasch et al., 2019), which uses the High-Order Methods Modeling Environment (HOMME) Spectral

96 Element dynamical core (Dennis et al., 2012). The dynamical core and the physics parametrizations are

97 computed on cubed-sphere grids with data stored at Gauss-Lobatto-Legendre (GLL) nodes. The EAMv1

98 standard low-resolution configuration has 30 spectral elements per cube face (ne30) and 4 GLL nodes per

99 spectral element (np4), corresponding to a horizontal grid spacing of ~100 km. The model has 72 vertical

100 layers with a vertical resolution of ~20 m near the surface and a vertical resolution higher than 200 m

101 below 1.5 km, and the model top reaches up to ~60 km ($\approx$ 0.1 hPa). The model uses an updated version of

102 the Zhang and McFarlane (1995) (ZM) deep convection scheme with a modified dilute plume calculation

103 (Neale et al., 2008), the Cloud Layers Unified By Binormals (CLUBB) scheme for turbulence, shallow

104 convection, and stratiform clouds (Bogenschutz et al., 2013; Golaz et al., 2002; Larson et al., 2002; Xie et

105 al., 2018), the version 2 of the Morrison and Gettelman (2008) (MG2) 2-moment cloud microphysics

106 scheme with a classical-nucleation-theory-based ice nucleation parameterization (Hoose et al., 2010;

107 Wang et al., 2014), the revised version of the four-mode version of the Modal Aerosol Module (MAM4)

108 (Liu et al., 2016; Wang et al., 2020), and the Rapid Radiative Transfer Model for GCMs (RRTMG)

109 (GCM: general circulation model) (Iacono et al., 2008; Mlawer et al., 1997).

110   MAM4 considers seven aerosol species: mineral dust, sea salt, marine organic matter (MOM), black

111   carbon (BC), primary organic matter (POM), secondary organic aerosol (SOA), and sulfate (SO_4) (Wang

112   et al., 2020). Dust emission is parameterized as a function of surface wind speed, soil erodibility, friction

113   velocity, and a friction velocity threshold following the scheme of Zender et al. (2003) in the land

114   component of E3SMv1. The emissions of sea salt and MOM are estimated from sea spray fluxes, which

115   are parameterized as a function of surface wind speed and sea surface temperature (Burrows et al., 2022).

116   Emissions of other aerosol species and precursor gases are prescribed using CMIP6 emission datasets

117   (Hoesly et al., 2018; Van Marle et al., 2017). The physical properties (including the size distribution,

118   density, and hygroscopicity) of the seven aerosol species are summarized in Burrows et al. (2022).

119   MAM4 represents aerosol particles in four modes with distinct size properties: Aitken mode,

120   accumulation mode, coarse mode, and primary carbon mode (Burrows et al., 2022; Liu et al., 2016; Wang

121   et al., 2020). The primary carbon mode is specified for freshly emitted BC, POM, and MOM, the aging of

122   which is treated explicitly — a feature different from the three-mode version of MAM (MAM3) (Liu et

123   al., 2012). The Aitken mode consists of sea salt, MOM, SOA, and SO_4, while all seven species can exist

124   in accumulation and coarse modes. MAM4 assumes that aerosol species are internally mixed within each

125   mode but externally mixed across different modes. Aerosol particles in each mode can suspend in the air

126   (i.e., interstitial aerosols) or exist in cloud droplets (i.e., cloud-borne aerosols). The evolution of aerosol

127   particles involves many physical and chemical processes, such as emissions, nucleation, coagulation,

128   condensation, convective transport, activation, dry deposition, wet scavenging, resuspension, and gas-

129   phase and aqueous chemistry. More details of these processes and their interactions with radiation and

130   cloud microphysics are described in Liu et al. (2012), Liu et al. (2016), Wang et al. (2020), and Zhang et

131   al. (2022a).

132   EAMv1 has been evaluated against observations and other ESMs in Xie et al. (2018), Rasch et al.

133   (2019), and Golaz et al. (2019). The simulation of aerosol properties and ERF_{aer} have been evaluated in

134   Table S1 and Figures S1-S2, Wang et al. (2020), Burrows et al. (2022), Feng et al. (2022), and Zhang et

135   al. (2022a). Our investigation focuses on comparing LR and RRM simulations, and the known model

136   biases, such as the dry biases over the Great Plains of the US, the Amazon region, and Southeast Asia

137   (Xie et al., 2018) and the cold bias between the 1950s and the 2000s (Golaz et al., 2019), are not expected

138   to affect the overall model sensitivity to the resolution change.

2.2 E3SMv1 LR and RRM simulations

139

140   In addition to the standard LR E3SMv1 simulation with a globally uniform resolution of ~100 km

141   for EAMv1 and the land component, we conduct an RRM simulation following the configuration of Tang

142   et al. (2019) with a relatively high-resolution mesh (~25 km) over the CONUS for the atmospheric and

143   land components (Figure 1). The simulation period is from October 1, 2015, to January 1, 2017, with the

144   first three months as model spin-up (Zhang et al., 2022a). The component set used in the simulations We

145   use the "FC5AV1C-04P2" compset in E3SMv1 for our study. FC5AV1C-04P2 comprises the coupling of

146   an active atmospheric component — EAMv1, an active land component (version 4.5 of the Community

147   Land Model — CLM4.5) (Oleson et al., 2013), a simplified active sea ice component, and a data ocean

148   model with prescribed historical sea surface temperature and sea ice fractions (Hurrell et al., 2008).

149   The atmospheric and land initial conditions in the LR simulation are derived from an earlier

150   E3SMv1 simulation, which has reached equilibrium. The RRM initial conditions are regridded from those

151   of the LR simulation to exclude the potential impact of distinct initial conditions on the simulation results.

152   Anthropogenic and biomass-burning emissions of BC, POM, and SO_4 and precursor gas sulfur dioxide

153   (SO_2) are from the CMIP6 emission inventory (Feng et al., 2020; Hoesly et al., 2018). Notably, we use

154   the emission data in 2014 instead of in 2016 due to the data availability of CMIP6. Dimethyl sulfide

155   (DMS) emissions in 1850, 2000, and 2100 are estimated from a coupled model simulation with a detailed

156   representation of DMS formation in the seawater (Wang et al., 2018). We obtain the DMS emissions in

157   2014 through linear interpolation of the emissions in 1850, 2000, and 2100. The 3-D SOA production

158   rates (implemented similarly to emissions) are derived from the simulation from Shrivastava et al. (2015).

159   Besides the PD LR and RRM simulations, we run two corresponding simulations with PI aerosol

160   emissions to calculate ERF_{aer}. The PI simulation configurations are the same as the corresponding PD

161   simulations except that emissions of BC, POM, SO_4, SO_2, DMS, and SOA (production) in 1850 are used

162   in the PI simulations.

163   We apply nudging globally in the LR and RRM simulations, which differs from Tang et al. (2019),

164   which used nudging only on the low-resolution meshes but not the high-resolution grids in CONUS. We

165   follow the nudging strategy from Zhang et al. (2014) and Sun et al. (2019), which demonstrated that a

166   simulation with constraint horizontal winds could reproduce the evolution characteristics of the observed

167   weather events and the model's long-term climatology. In addition, it has been corroborated that nudged

168   simulations with a relatively short simulation period (e.g., one year) can reproduce the annual mean

169   changes in aerosol burdens and optical depths caused by anthropogenic aerosols in the E3SM

170   Atmospheric Model Intercomparison Project (AMIP) simulations (Zhang et al., 2022a). The short nudged

171   simulations also have a similar estimate of ERF_{aer} as the AMIP-type free-running simulations (Zhang et

172   al., 2022a). Moreover, by constraining the large-scale circulation, nudging helps ~~to~~ suppress the noises

173   caused by the chaotic response to model changes and facilitates the comparison between the LR and RRM

174   simulations. Similarly, nudging is also used to estimate ERF_{aer}, as recommended by previous studies

175   (Kooperman et al., 2012; Sun et al., 2019; Zhang et al., 2014). In short, nudging helps increase the signal-

176   to-noise ratio and identify the impact caused by regional refinement more quickly. In our simulations, the

177   horizontal winds are nudged toward the European Centre for Medium-Range Weather Forecasts

178   Reanalysis v5 (ERA5) (Hersbach et al., 2020) with a relaxation time of 6 hours (Zhang et al., 2022b). To

179   avoid the errors caused by vertical interpolation-extrapolation from ERA5 to E3SM vertical levels, we

180   don't apply nudging for model levels below 950 hPa and above 10 hPa.

181   Several parameters differ between the E3SMv1 standard LR and CONUS RRM default

182   configurations. For example, the time step for most physical processes and the coupling between physics

183   and dynamics is 30 minutes in the LR configuration. In comparison, CONUS RRM uses a time step of 15

184   minutes. Many physical processes are sensitive to the time step and parameter setting (Wan et al., 2015;

185   Wan et al., 2021; Zhao et al., 2013). Our sensitivity tests show substantial differences in the aerosol mass

186   and energy budgets even outside of the refined region when the respective default configurations are used

187   in the LR and RRM simulations, which is mainly attributed to their distinct physical time steps (not

188   shown). Therefore, it would be better to keep the tuning parameters and time step the same between the

189   LR and RRM simulations to isolate the regional refinement effect (horizontal resolution sensitivity), as

190   recommended by earlier studies (Caldwell et al., 2021; Ma et al., 2015). Therefore, for the LR simulation,

191   we use the time step of 15 minutes and the parameter setting from the default CONUS RRM

192   configuration. With such changes, LR shares the same configuration as RRM, except for regional

193   refinement around CONUS (Figure 1) and resolution-relevant input files (e.g., topography and nudging-

194   prescribed wind fields). As expected, the results are very close between the LR and RRM simulations in

195   the low-resolution (~100 km) areas (not shown), facilitating our subsequent investigation of the impacts

196   of regional refinement on the aerosol mass budget and the aerosol forcing over CONUS.
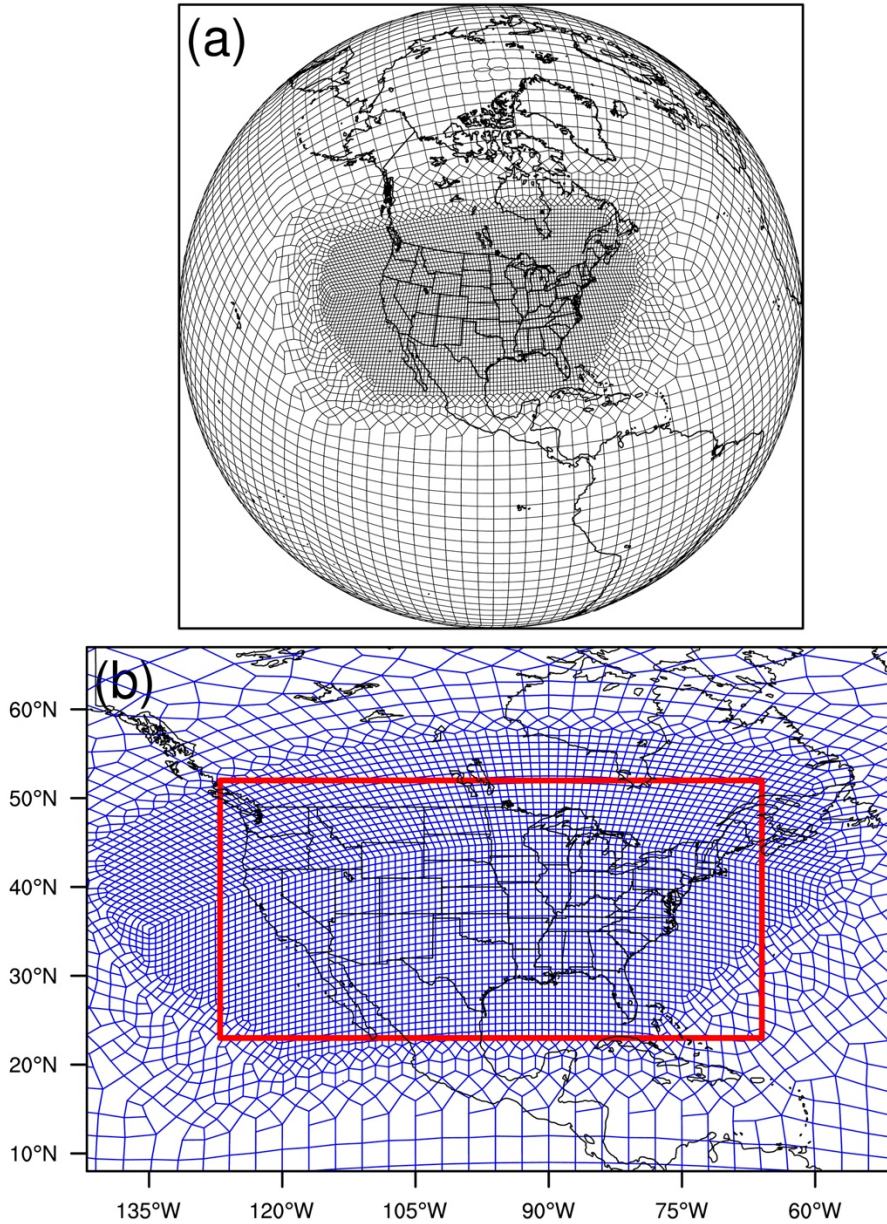
197
198 Figure 1. E3SMv1 RRM domain (spectral elements) in (a) an orthographic projection and (b) a cylindrical
199 equidistant projection. (a) and (b) show the boundaries of spectral element grids. The red rectangle in (b) outlines
200 the region we focus on in the following analyses, referred to as the RRM region.

201 3 Results and Discussions

202   We focus our analysis on the refined region, as outlined by the red box in Figure 1b (hereafter

203 referred to as the RRM region), and the annual mean simulation results in 2016 unless stated otherwise.

204   The LR and RRM simulation results have been regridded to 1° × 1° to facilitate their comparison unless

205   otherwise indicated.

3.1 Aerosol natural sources

207   Table 1 summarizes the annual mean sources and burdens of the seven aerosol species in the RRM

208   region from the LR and RRM simulations. We find the largest relative differences in the sources and mass

209   burden of the natural wind-driven aerosols between the RRM and LR simulations. With higher horizontal

210   resolution, the RRM simulation produces more dust (154%), sea salt (13%), and MOM (10%) emissions

211   than LR. The dust emission enhancement by RRM is concentrated in several inland regions with high

212   dust emissions, especially in the Mohave and Sonoran deserts (referred to as Region 1) and the northern

213   North American Prairie (referred to as Region 2) (Figures 2a and 2b). In comparison, the increases in sea

214   salt and MOM emissions mainly occur around the coastal lines (Figures 2c-2f). That dust emissions

215   increase with finer model resolutions has been identified in earlier studies (Caldwell et al., 2019; Feng et

216   al., 2022; Ridley et al., 2013), which attributed the increase to more frequent occurrences of strong winds

217   in high-resolution simulations. Dust emissions are nonlinearly correlated with surface winds and are

218   particularly sensitive to strong winds (Zender et al., 2003). We find larger (11.2~~7.8~~%) annual mean

219   surface wind speeds and more frequent strong winds in Region 1 in the RRM simulation compared to the

220   LR simulation (Figures 3c~~a~~ and 3d~~e~~), which can explain the dust emission increase in Region 1 under

221   regional refinement (Figure 2b). However, in Region 2, the annual mean surface wind speeds differ

222   slightly (2.2~~1.6~~%) between the RRM and LR simulations. Besides, the probability density functions

223   (PDFs) of wind speed in Region 2 are similar between the two simulations (Figures 3c~~a~~ and 3e~~d~~), as well

224   as the PDFs of friction velocity (not shown), indicating that surface winds and friction velocities alone

225   cannot explain the dust emission enhancement in the RRM simulation. In addition to surface winds and

226   friction velocity, soil moisture can also influence dust emissions by improving the friction velocity

227   threshold (Namikas and Sherman, 1997; Zender et al., 2003). Therefore, high soil moisture may inhibit

228 saltation and thus reduce dust emissions. We find lower (-7.1%) volumetric soil water content in the

229 surface layer in Region 2 in the RRM simulation than in the LR simulation (Figure 3b), which is

230 consistent with the dust emission increase in the region by RRM (Figure 2b). The reduced surface soil

231 water content in Region 2 is likely related to less precipitation (-3.0%) in the RRM simulation compared

232 to the LR simulation (Figure 4c).

233 **Table 1.** Total annual mean sources and burden in the RRM region for the seven aerosol species

	Sources			Burden		
	RRM / Tg yr^{-1}	LR / Tg yr^{-1}	Relative diff[1] / %	RRM / Tg	LR / Tg	Relative diff / %
Dust	22.3	8.79	154	0.126	0.0910	39
Sea salt	39.4	34.9	13	0.0875	0.0782	12
MOM	0.192	0.175	10	0.00114	0.00104	9.8
BC	0.268	0.268	0.0030	0.00446	0.00446	-0.050
POM	1.15	1.15	0.022	0.0287	0.0286	0.30
SOA	2.70	2.68	0.72	0.0859	0.0857	0.26
SO$_4$[2]	1.74	1.69	2.8	0.0216	0.0215	0.41

234 [1]$Relative\ diff = (RRM/LR - 1) \times 100\%$.
235 [2]SO$_4$ is represented in the mass of sulfur (TgS y^{-1} for sources and TgS for burden). Besides direct anthropogenic
236 emissions of SO$_4$, other SO$_4$ sources include gas-aerosol exchange, aqueous-phase production (aqueous-phase
237 chemistry and cloud water uptake), and new particle formation.

238   As mentioned above, sea salt and MOM emissions are related to surface wind speed and sea surface

239 temperature (Burrows et al., 2022; Liu et al., 2012). We attribute the increased sea salt and MOM

240 emissions in the RRM simulation to enhanced surface wind speeds at the finer model resolution, as shown

241 in Figure 3a. In addition, since sea salt and MOM are only emitted over the ocean, the distinct land-ocean

242 boundaries may also partially contribute to the discrepancies in sea salt and MOM emissions between the

243 RRM and LR simulations.
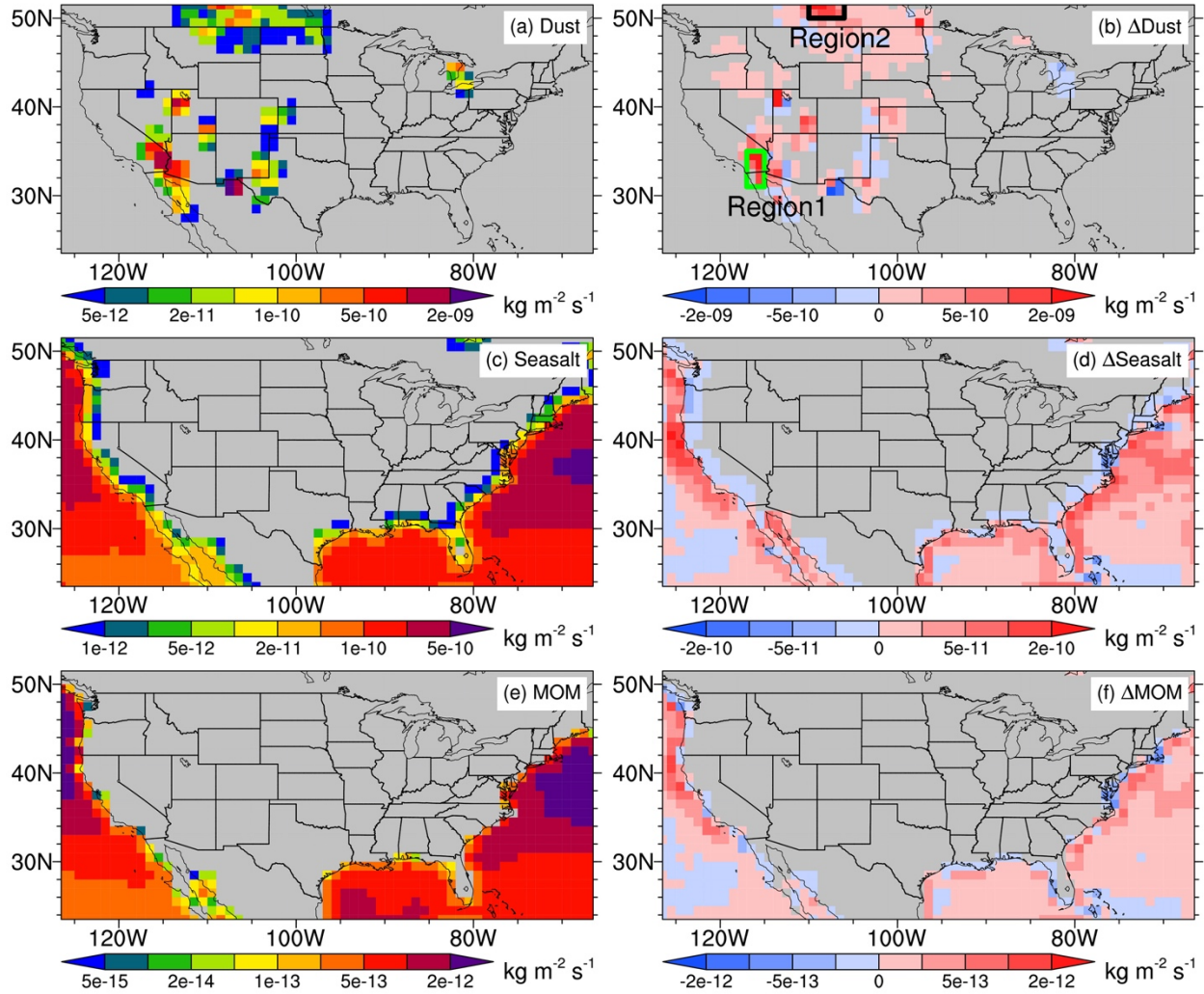
244
245 Figure 2. Left column: spatial distributions of annual mean sources of (a) dust, (c) sea salt, and (e) MOM from the
246 LR simulation. Right column: the same as the left column but for the absolute differences between the RRM and LR
247 simulations (RRM-LR). The green and black boxes in (b) highlight two subregions with substantial changes in dust
248 emissions when applying regional refinement. Region 1 is around the Mohave and Sonoran deserts, and Region 2 is
249 in the northern North American Prairie.

250
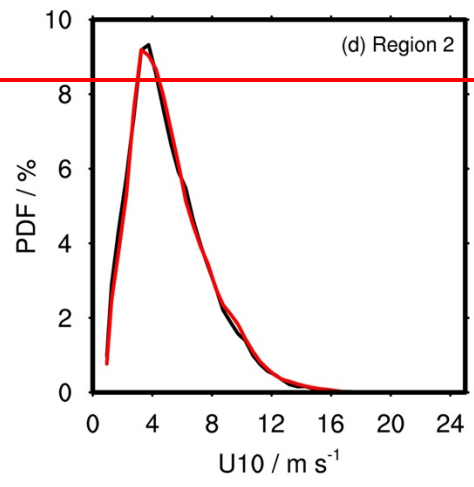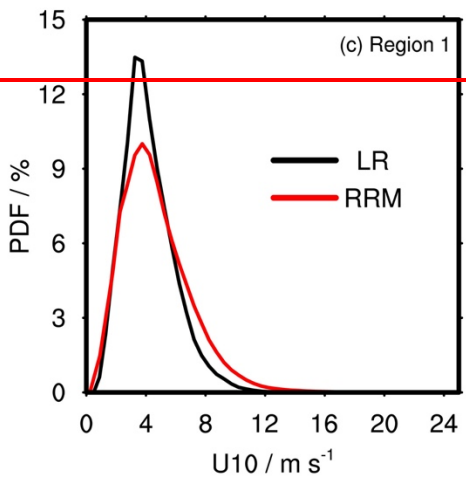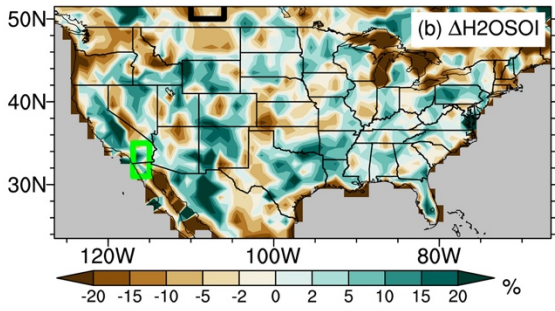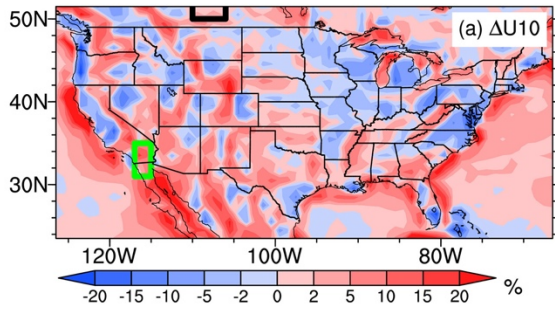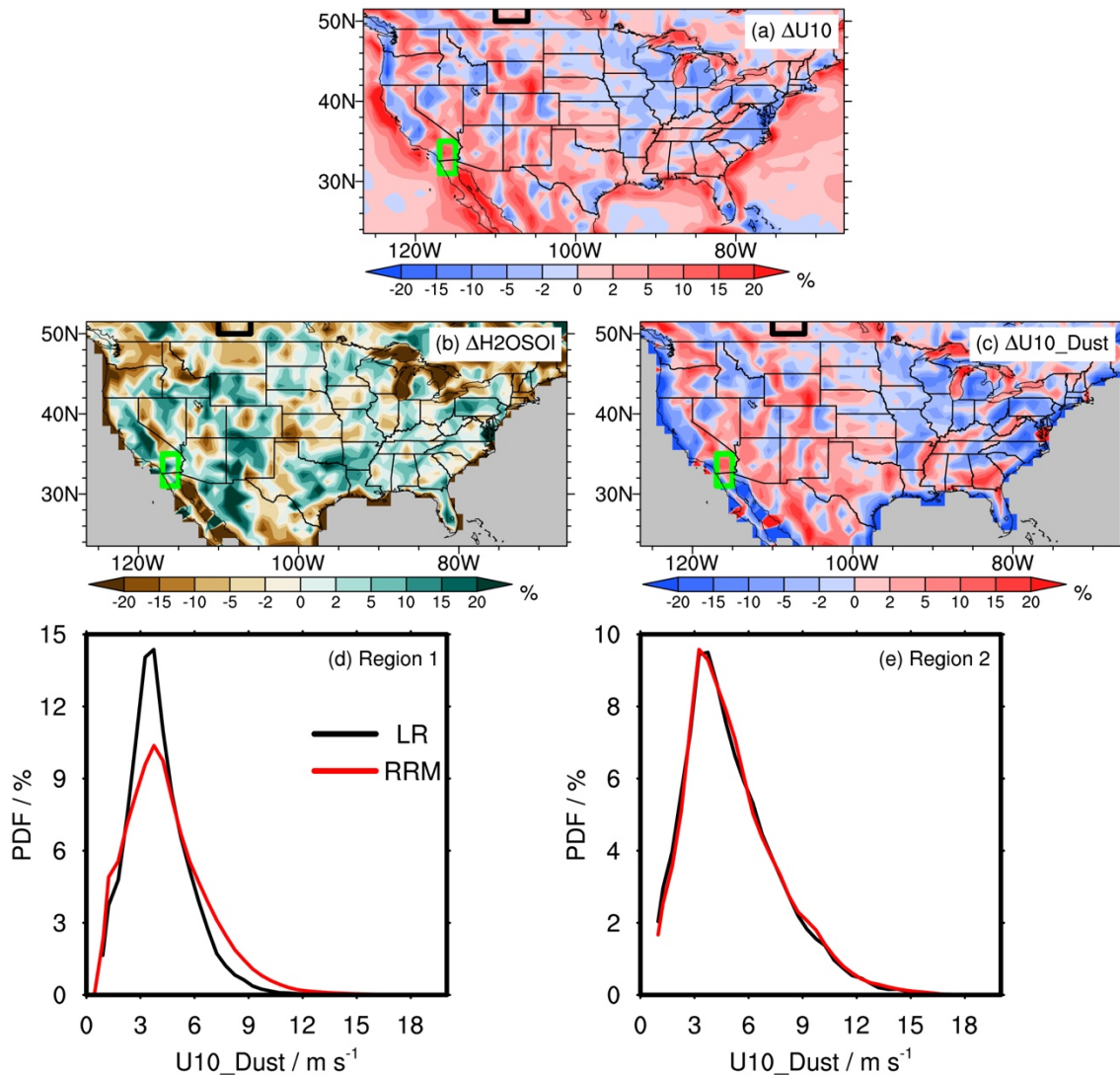
Figure 3. Spatial distributions of the relative differences in annual mean (a) 10-m wind speed from the E3SMv1 atmospheric component (U10), and (b) surface-layer volumetric soil water content (H2OSOI), and (c) 10-m wind speed used in the dust emission parameterization (U10_Dust) between the RRM and LR simulations (RRM-LR). The green and black boxes in (a), (b), and (cb) are the same as those in Figure 2b. (de, ed) Probability density functions (PDFs) of U10_Dust in (de) Region 1 and (ed) Region 2. The black lines are for the LR simulation, while the red lines are for the RRM simulation. U10_Dust on native model grids with an output frequency of 15 minutes is used to derive the corresponding PDF. Notably, U10_Dust is slightly different from U10, which considers the convective gustiness effect.

3.2 Aerosol wet scavenging by convective vs. large-scale precipitation

In the RRM region, wet scavenging is the primary sink for most aerosol species in both simulations except for dust and sea salt, the sinks of which are dominated by dry deposition. To understand the impact of ~~RRM~~ horizontal grid spacing on aerosol wet scavenging, it is necessary first to investigate how precipitation differs between the LR and RRM simulations.

Figure 4 evaluates the LR and RRM simulated precipitation against the observational Stage IV data. Stage IV is a radar-based precipitation product with rain-gauge bias adjustment and has a native resolution of 4 km (Lin and Mitchell, 2005). We regrid the Stage IV data to $1° \times 1°$ for comparison with our simulation results. Both simulations can capture the observed east-west precipitation gradient in the US east of the Rocky Mountains. The spatial correlation coefficient between the LR simulation and Stage IV is 0.52, similar to that between RRM and Stage IV. Moreover, most observed precipitation events in the central-eastern US (red box in Figure 4d) are well simulated by the LR and RRM simulations according to the Hovmöller diagrams of meridionally averaged daily precipitation rates in Figure 5, which is attributed to the appropriate nudging strategy applied to the simulations. However, apparent dry biases are found near the coastal areas of the southern US in the LR simulation (Figure 4e). By producing more precipitation than the LR simulation around the US coastal areas, RRM can reduce the dry bias in the southern coastal regions. However, its precipitation is still much lower than observed (Figure 4f). Minor dry biases are also found in the northern Great Plains in both simulations. The model dry biases in the southern and northern Great Plains may be due to the limitation of E3SM in predicting extreme precipitation events, such as mesoscale convective systems (Feng et al., 2021; Wang et al., 2021), which is the dominant precipitation contributor in the Great Plains (Li et al., 2021). A noticeable improvement of the RRM simulation compared to the LR simulation is the production of more frequent heavy precipitation (> 7.6 mm h^{-1}), which is mainly attributed to the intensification of large-scale precipitation (Figure 6), consistent with the results from Caldwell et al. (2019). More frequent heavy precipitation can

284 partially alleviate the "too frequent, too weak" problem in low-resolution E3SM simulations (Caldwell et

285 al., 2019). However, our result contradicts Tang et al. (2019), which found more light precipitation but

286 less heavy precipitation as model horizontal resolution increases. It may be because Tang et al. (2019)

287 didn't apply nudging to their low-resolution and RRM simulations, and precipitation varied much

288 between the two simulations.
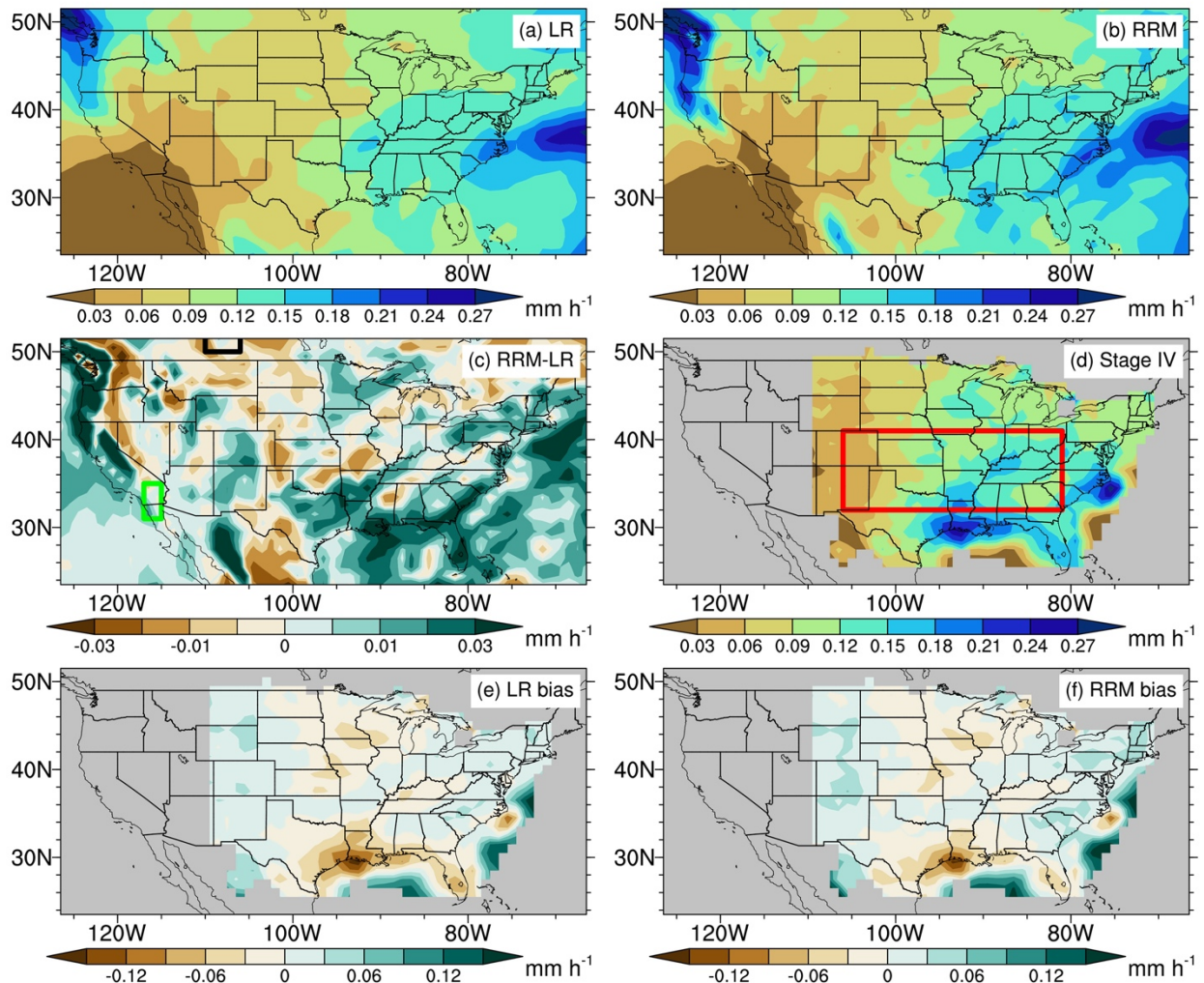
289
290 Figure 4. (a-c) Spatial distributions of annual mean total precipitation rates (large-scale and convective) for the (a)
291 LR and (b) RRM simulations and (c) their differences (RRM-LR). The green and black boxes in (c) are the same as
292 those in Figure 2b. (d-f) Spatial distributions of annual mean precipitation from Stage IV and the precipitation bias
293 of the LR and RRM simulations against Stage IV. The regional mean biases of the LR and RRM simulations are
294 0.004 mm h^{-1} and 0.010 mm h^{-1} compared to Stage IV with a regional mean precipitation of 0.107 mm h^{-1}. It is
295 noteworthy that the data quality of Stage IV is poor over the open ocean and the western US due to limited radar
296 coverage. The Hovmöller diagram in Figure 5 is based on the red box in (d).
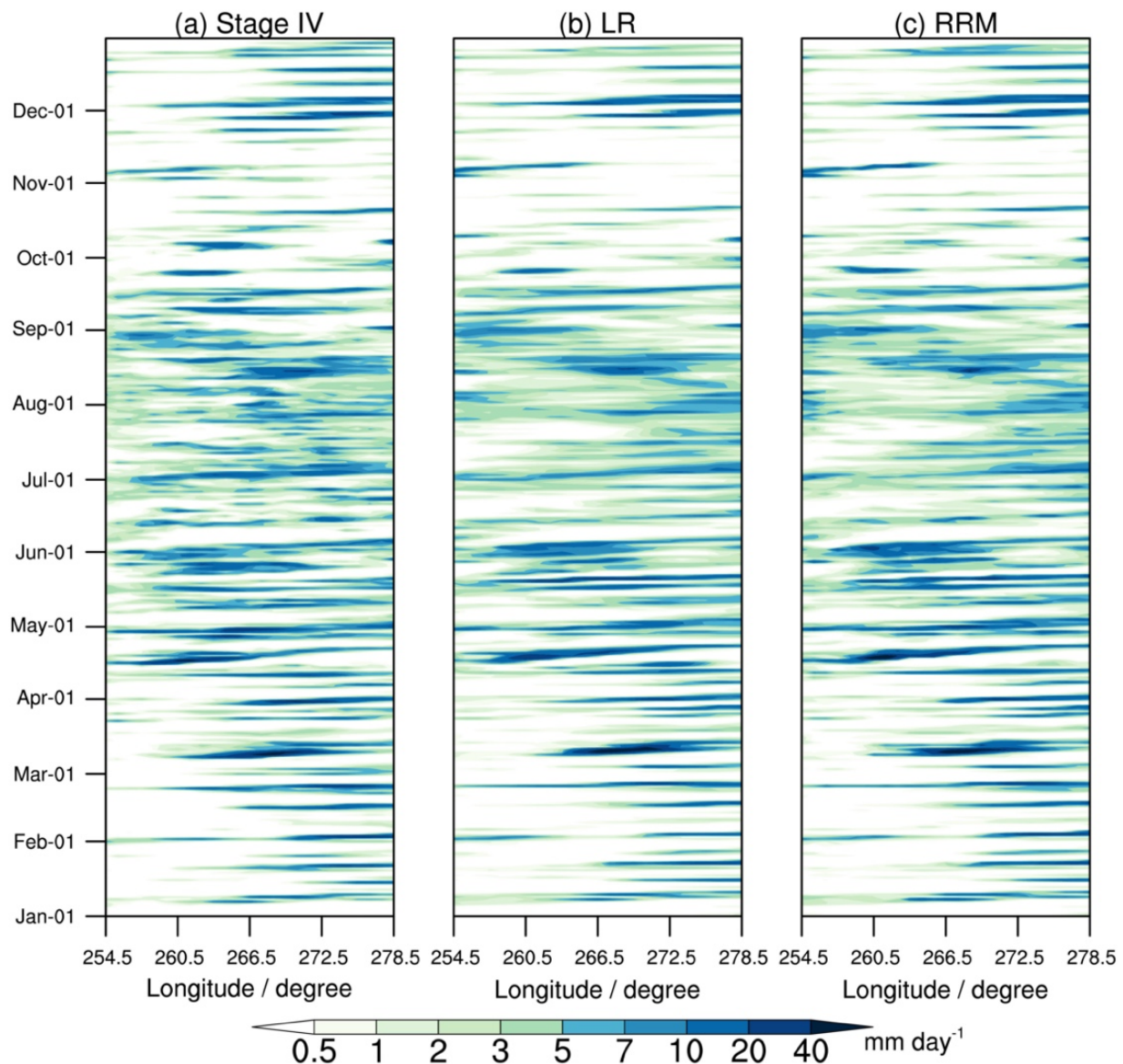
Figure 5. Hovmöller diagrams of meridionally averaged daily precipitation rates in the red box of Figure 4d for (a) Stage IV, (b) the LR simulation, and (c) the RRM simulation in 2016. The centered pattern correlation coefficient between LR and Stage IV is 0.28, the same as that between RRM and Stage IV. The root-mean-square errors of LR and RRM are 5.3 mm day^{-1} and 5.5 mm day^{-1}, respectively, against Stage IV.
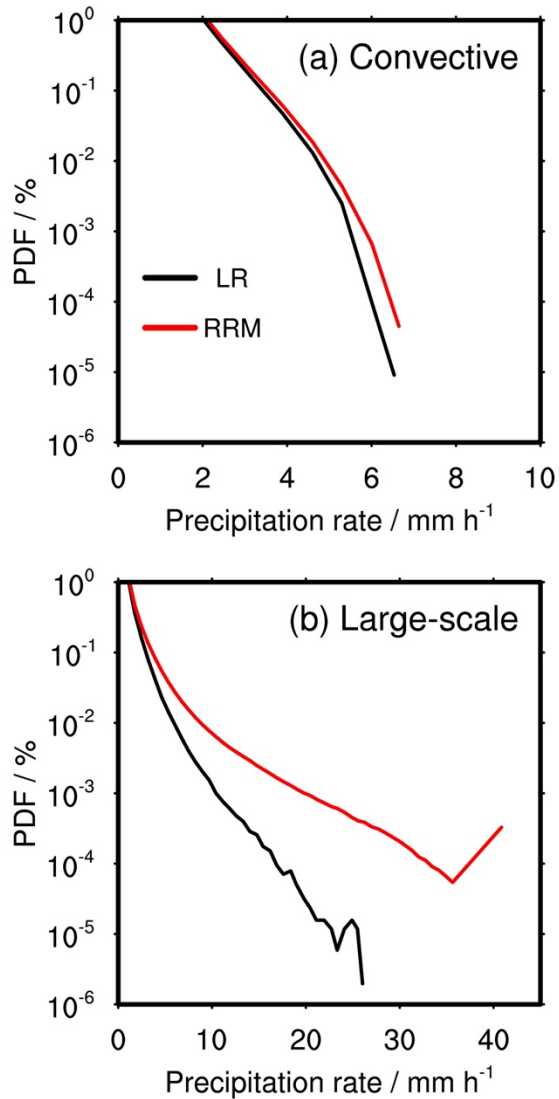
302
303 Figure 6. Probability density functions (PDFs) of (a) convective and (b) large-scale precipitation rates in the RRM
304 region for the LR (black lines) and RRM (red lines) simulations. Precipitation on native grids with an output
305 frequency of 15 minutes is used to calculate the corresponding PDF.

306   In addition to affecting total precipitation rates, the model resolution notably changes the partitioning

307 between large-scale precipitation (that is computed by the MG2 cloud microphysics parameterization) and

308 deep convective precipitation (that is computed by the ZM deep convection parametrization). As model

309 resolution increases, more precipitation can be resolved, which leads to an increase in large-scale

310 precipitation and a decrease in convective precipitation (Figures 7a and 7b) (Tang et al., 2019).

311   In E3SMv1, aerosol wet removal by large-scale and convective precipitation is comprised of in-

312 cloud scavenging, which involves the activation of interstitial aerosol particles (IAPs) and the subsequent

313 removal of cloud-borne aerosol by precipitation, and below-cloud scavenging accounting for the removal

314 of IAPs by precipitation via impaction and Brownian diffusion (Liu et al., 2012; Wang et al., 2013). In-

315 cloud scavenging is the dominant process for all aerosol species in the RRM region, accounting for ~80%

316 of the wet removal of sea salt and dust and more than 98% of the other aerosol species (not shown).

317   EAMv1 uses two different parameterizations to treat aerosol wet scavenging by large-scale clouds

318 and deep convective clouds. Here, "large-scale clouds" refer to clouds represented by the CLUBB and

319 MG2 parameterizations, and "deep convective clouds" refer to clouds represented by the ZM deep

320 convection parameterization. In large-scale clouds, aerosol activation is parameterized as a function of

321 subgrid vertical velocity (W_{sub}), aerosol properties, and environmental conditions (Abdul-Razzak and

322 Ghan, 2000). The first-order loss rates of aerosol are computed by multiplying a solubility factor by the

323 first-order loss rate of cloud water, which is computed as a function of cloud fraction, cloud water, and

324 precipitation production rate profiles (Barth et al., 2000; Rasch et al., 2000). In deep convective clouds,

325 the cloud-borne aerosol mixing ratios are computed by multiplying interstitial aerosol mixing ratios by

326 the prescribed convective-cloud activation fractions, which depend on aerosol modes and species to

327 represent the hygroscopicity (Liu et al., 2012; Wang et al., 2013). The solubility factor is a tunable

328 parameter, and the model uses different solubility factors for large-scale and deep convective clouds (Liu

329 et al., 2012; Wang et al., 2013).

330   Therefore, the change in the partitioning between large-scale and deep convective precipitation

331 should make a difference in aerosol wet removal. Taking SO_4 as an example, Figures 7c and 7d show a

332 significant increase in in-cloud scavenging of SO_4 by large-scale precipitation but a noticeable decrease

333 by deep convective precipitation in the RRM simulation compared to the LR simulation. The changing

334 patterns of in-cloud scavenging by large-scale and deep convective precipitation are consistent with the

335 changes in the corresponding type of precipitation rates. Figure 8 summarizes the relative differences in

336 regional mean large-scale and deep convective in-cloud scavenging of different aerosol species in the

337 RRM region between the RRM and LR simulations. Due to the increase in large-scale precipitation (28%)

338 and the decrease in deep convective precipitation (-16%) in the RRM region, the large-scale in-cloud

339 scavenging increases and the deep convective in-cloud scavenging reduces for all aerosol species but dust

340 in the RRM simulation compared to the LR simulation. Dust exhibits a different response because dust

341 emission is 154% higher in the RRM simulation than in the LR simulation. With the significant increase

342 of dust emission and loading in the atmosphere in the RRM simulation, the wet removal of dust by both

343 large-scale and deep convective clouds are higher than that in the LR simulation, even though the deep

344 convective precipitation rate is lower.
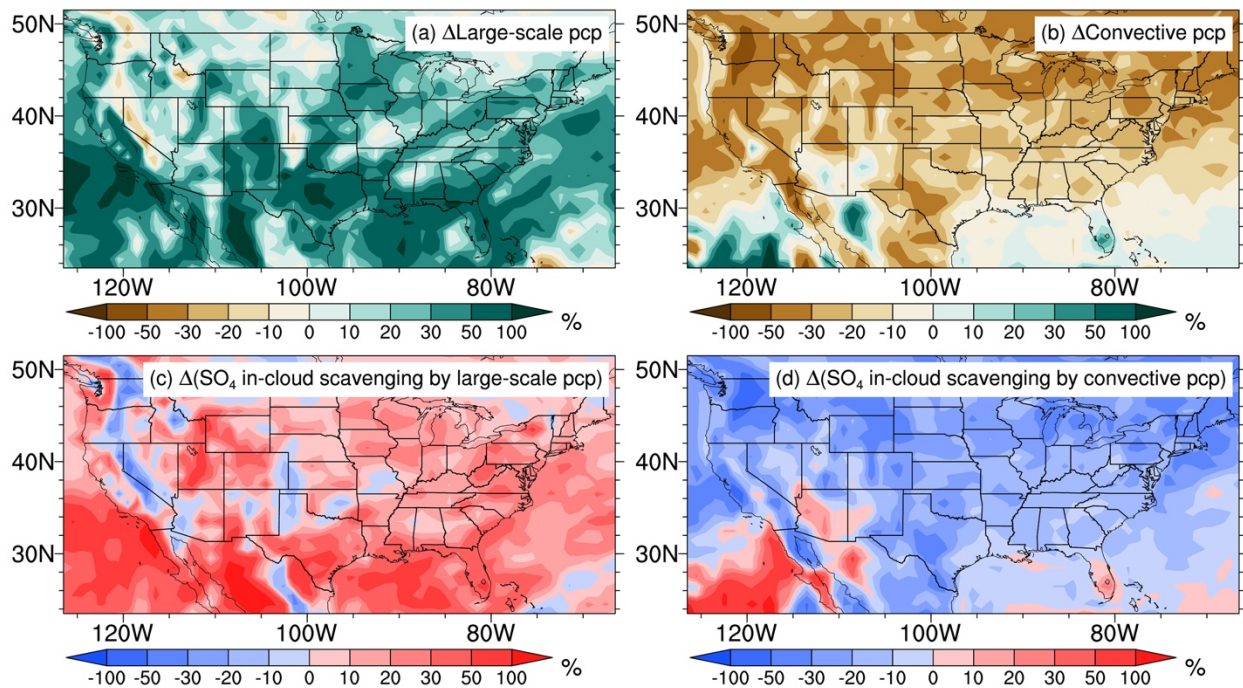
345
346 Figure 7. (a, b) Spatial distributions of the relative differences in annual mean (a) large-scale and (b) convective
347 precipitation between the RRM and LR simulations. (c-d) same as (a) and (b) but for in-cloud scavenging of SO_4 by
348 (c) large-scale and (d) convective precipitation.
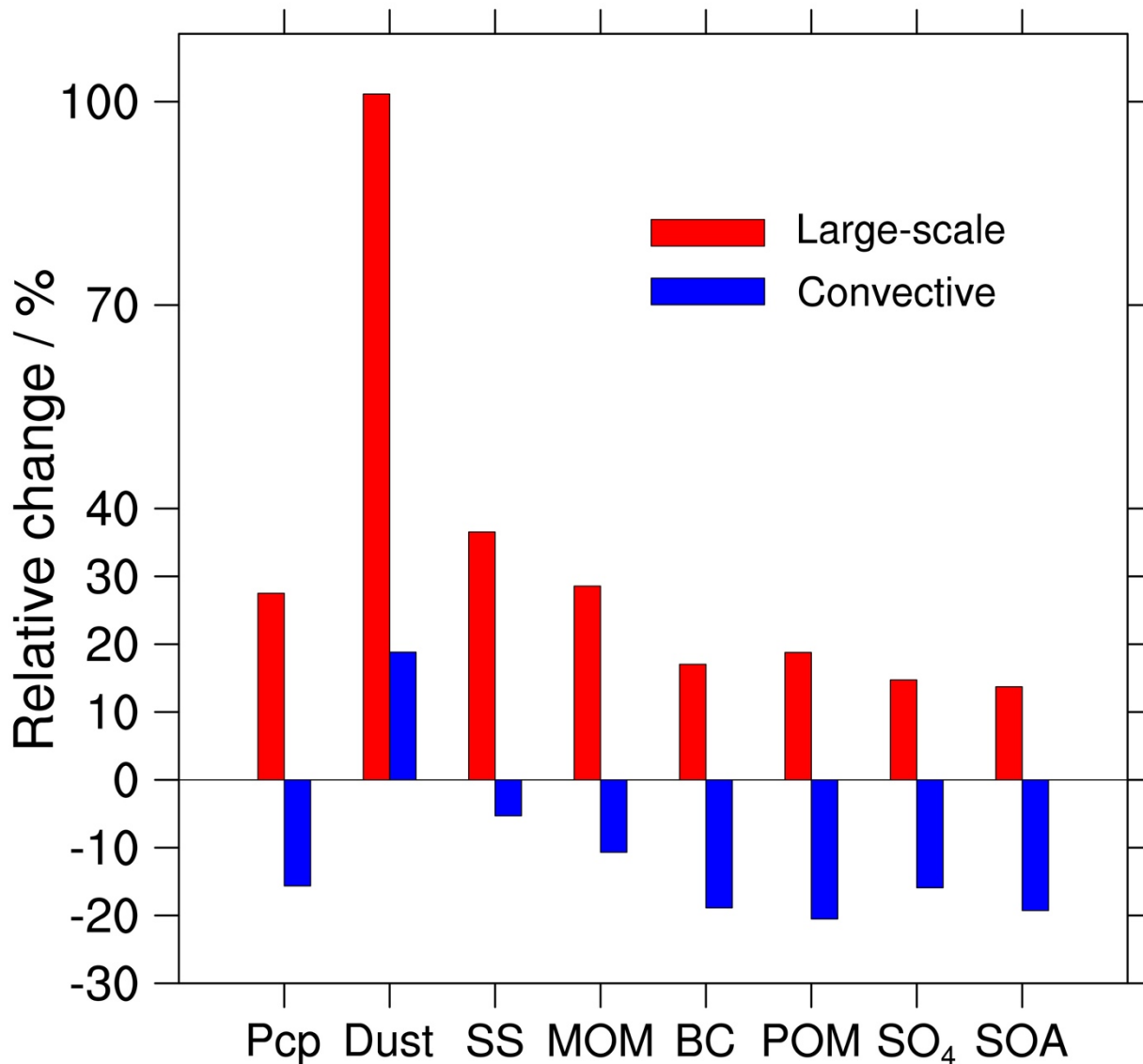
349
350 Figure 8. Relative differences in annual regional mean large-scale and convective precipitation and in-cloud
351 scavenging of different aerosol species by large-scale and convective precipitation between the RRM and LR
352 simulations. "Pcp" refers to precipitation, and "SS" denotes sea salt.

3.3 Aerosol chemical production

354   As expected, anthropogenic aerosol emissions (e.g., BC, POM, and SOA) prescribed by offline

355 emission inventories are almost the same between the RRM and LR simulations. However, the SO_4

356 source in the RRM simulation is 2.8% higher (Table 1). MAM4 considers four source terms for sulfate

357 aerosol. Two primary sources of SO_4 are gas-aerosol exchange and aqueous-phase production (Figure

358 S13), which contribute to 31% and 63%, respectively, in the RRM region. The other two minor source

359 terms are (1) direct emission of sulfate aerosol and (2) new particle formation (NPF) (Figure S~~1~~3),

360 accounting for about 5% and 1% of the total source. Figures 9a and 9c show the spatial distributions of

361 SO_4 production via the two major pathways from the LR simulation, generally consistent with the

362 distributions of precursor gases (sulfuric acid gas vapor (H_2SO_4) and SO_2 in Figures S~~2~~4a and S~~2~~4b) with

363 one peak in the northeastern US and another peak around southwestern Texas. The RRM simulation

364 generally produces more SO_4 via aqueous-phase production (6.2% on average over the RRM region) but

365 less via gas-aerosol exchange (-3.0%) than the LR simulation (Figures 9b and 9d). Figures 9e-9f show

366 that increasing resolution leads to significantly lower (-13.3%) NPF of SO_4.

367   SO_4 production via gas-aerosol exchange and NPF positively correlates with the H_2SO_4

368 concentration (Liu et al., 2012). We find a lower (-5.5%) H_2SO_4 concentration in the RRM than in the LR

369 (Figure S~~3~~5a), which can explain the reduction of SO_4 production via gas-aerosol exchange and NPF

370 (Figure S~~1~~3). The source of H_2SO_4 is the oxidation of gas-phase SO_2 by hydroxyl radical (OH) (Figure

371 S~~1~~3). In our E3SMv1 configuration, OH concentrations are prescribed, and the reaction rate constants of

372 SO_2 and OH are similar between the RRM and LR simulations (not shown). Therefore, the H_2SO_4

373 production is dominated by the gas-phase SO_2 concentration, which shows a reduction (-2.3%) in the

374 RRM compared to the LR (Figure S~~3~~5b). The sources of gas-phase SO_2 include direct emissions and the

375 oxidation of DMS by OH and nitrate radical (NO_3) (Figure S~~1~~3). DMS and SO_2 emissions are read from

376 emission inventories, and the reaction rate constants of DMS + OH and DMS + NO_3 are close between

377 the RRM and LR simulations. Therefore, the gas-phase SO_2 source is similar between the two

378 simulations, and we need to understand the sinks of gas-phase SO_2 to explain the general reduction of

379 gas-phase SO_2 concentrations in the RRM simulation.
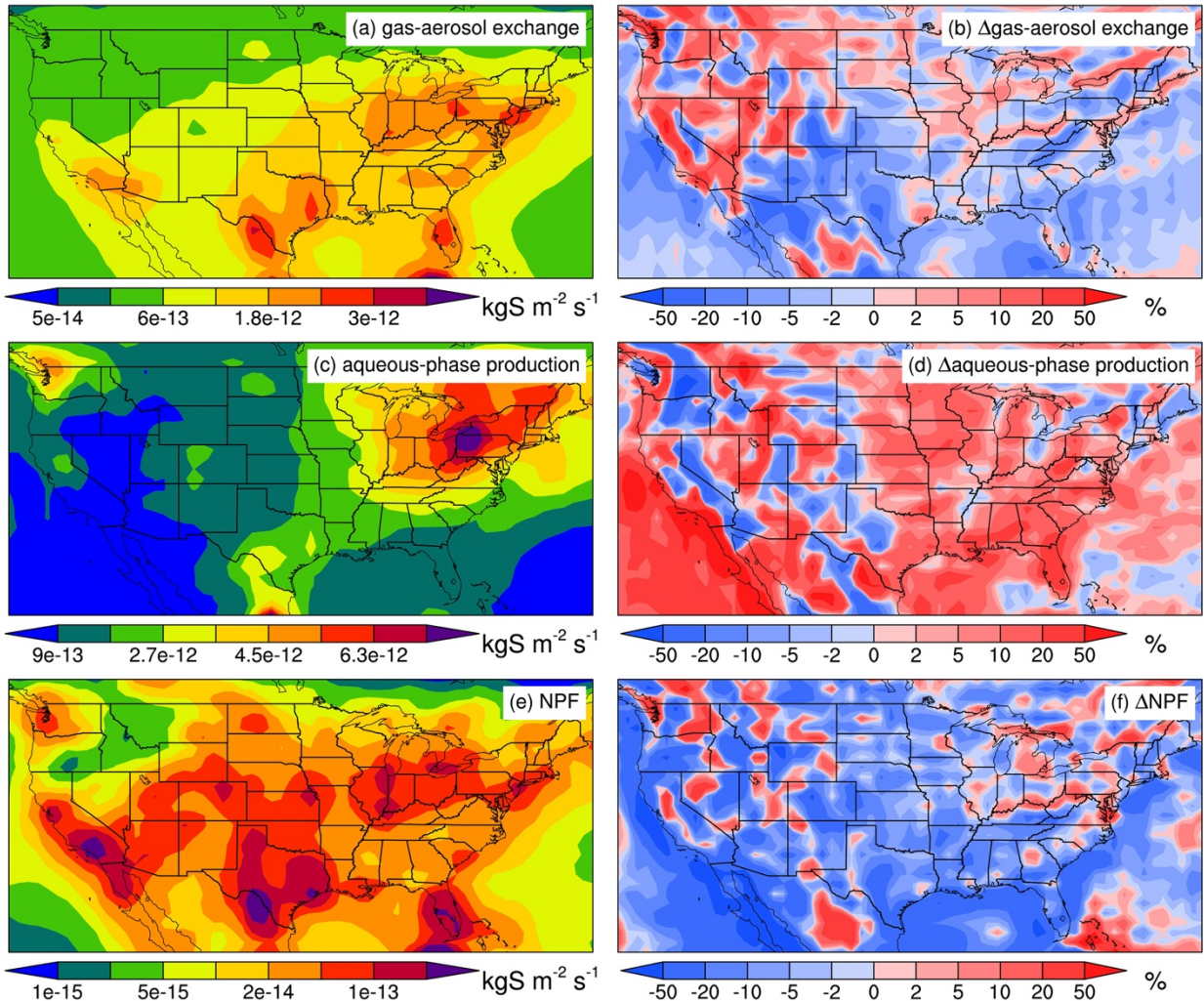
Figure 9. Left column: spatial distributions of annual mean SO_4 sources from (a) gas-aerosol exchange, (c) aqueous-phase production, and (e) NPF in the LR simulation. Right column: the same as the left column but for the relative differences between the RRM and LR simulations.

We find that dry and wet deposition cannot explain the general reduction of gas-phase SO_2 concentrations in the RRM compared to the LR (not shown). Another major sink of gas-phase SO_2 is the oxidation of SO_2 by hydrogen peroxide (H_2O_2) and ozone (O_3) to form SO_4 via aqueous-phase chemistry (Figures 10c, 10e, and S~~1~~3). Another process to produce SO_4 in the aqueous-phase chemistry module of E3SMv1 is the cloud water uptake of H_2SO_4 (Figures 10a and S~~1~~3). All three pathways are related to large-scale cloud liquid water content (LWC) (LWC at 700 hPa shown in Figure S~~2~~4c). The RRM simulation generally produces a larger LWC than the LR simulation (700 hPa shown as an example in

391   Figure S35c). Therefore, the cloud water uptake of H_2SO_4 is enhanced in the RRM simulation (Figures

392   10b and S13).

393   The aqueous-phase oxidation of SO_2 by H_2O_2 and O_3 would also be expected to increase with higher

394   LWC in the RRM simulation. However, we find a slight reduction (-1.2%) in SO_4 production via the O_3

395   pathway (Figure 10f). In contrast, the H_2O_2 pathway is enhanced by 17.0% in the RRM simulation

396   compared to the LR simulation (Figure 10d).

397   The H_2O_2 and O_3 pathways differ in two aspects. First, the O_3 concentrations are prescribed, while

398   the H_2O_2 concentrations are prognostic in our E3SMv1 configuration (Figures S13 and S24e). Second, the

399   O_3 pathway is highly sensitive to the pH of the cloud water (proton (H^+) concentrations at 700 hPa shown

400   in Figure S24d), while the H_2O_2 pathway is hardly affected by pH (Seinfeld and Pandis, 2016). We find

401   that the gas-phase H_2O_2 concentrations are generally slightly higher in the RRM than the LR (Figure

402   S35e), even though the improved H_2O_2 pathway should consume more H_2O_2 under regional refinement.

403   The budget analysis (not shown) indicates that the reduction of the gas-phase H_2O_2 wet removal in the

404   RRM simulation contributes to the slightly enhanced H_2O_2 concentrations (Figures S13, S24f, and S35f).

405   The reduced wet removal is related to decreased net rain production (mainly convective) used in the wet

406   deposition parameterization of gas species (not shown). Notably, the oxidation of SO_2 by H_2O_2 releases

407   H^+ into cloud water (Figure S13). With increased H_2O_2 concentrations, we expect higher H^+

408   concentrations ($[H^+]$) in large-scale clouds in the RRM simulation than in the LR simulation, as shown in

409   Figure S35d. Slightly higher $[H^+]$ (lower pH) would suppress the aqueous-phase oxidation of SO_2 by O_3

410   significantly (Seinfeld and Pandis, 2016). These results explain why the O_3 pathway is suppressed slightly

411   even though LWC increases in the RRM simulation compared to the LR simulation.

412   In short (Figure S13), higher LWC leads to more SO_4 production via cloud water uptake and the

413   aqueous-phase oxidation of SO_2 by H_2O_2. However, the oxidation of SO_2 by O_3 is slightly suppressed due

414   to the combination of larger LWC and lower pH. Finally, the total aqueous-phase SO_4 production is

415 enhanced in the RRM, which consumes more SO_2 and leads to lower gas-phase SO_2 concentrations

416 compared to the LR.
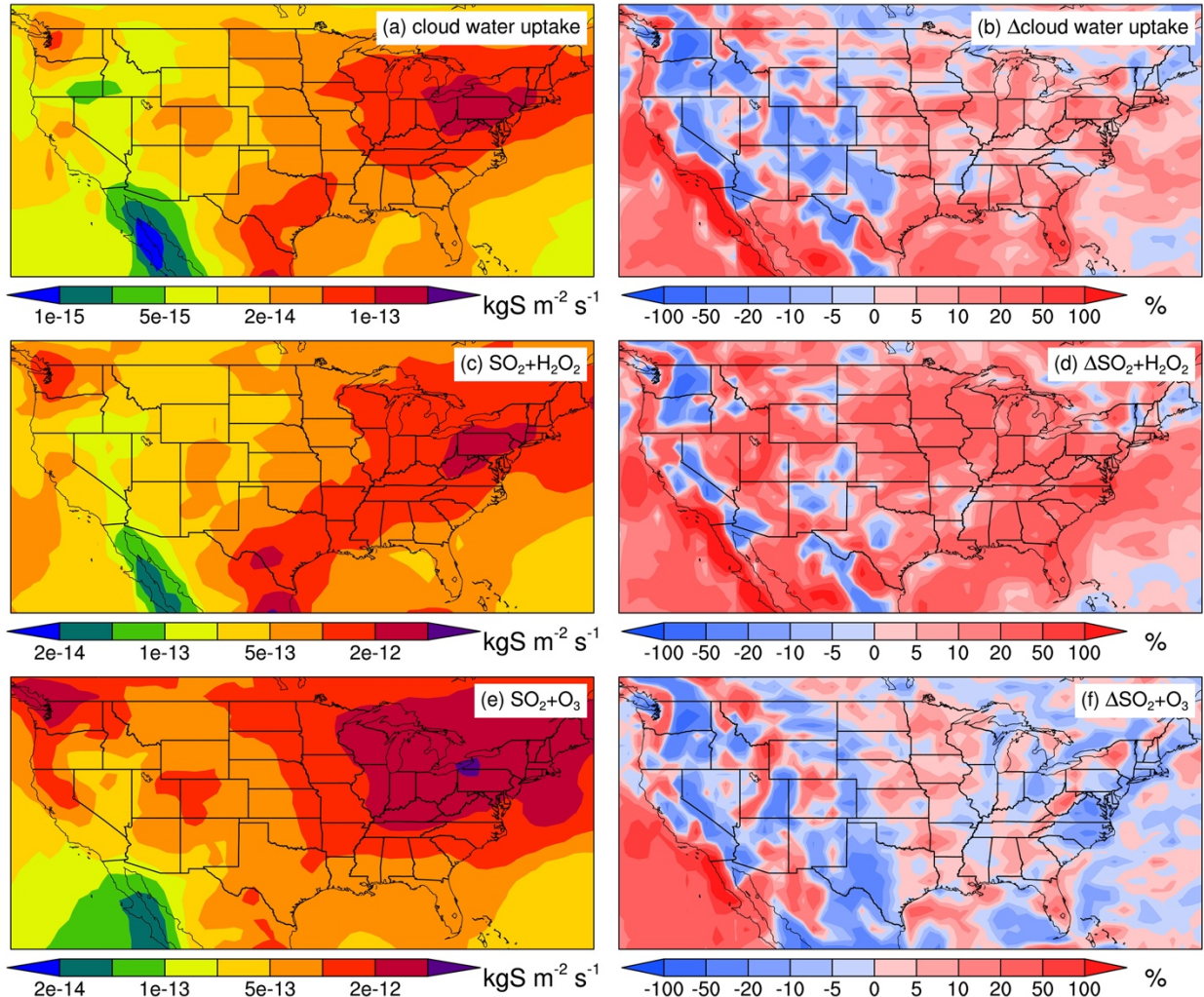
417
418 Figure 10. Left column: spatial distributions of annual mean SO_4 aqueous-phase productions through (a) cloud water
419 uptake, (c) the H_2O_2 oxidation pathway, and (e) the O_3 oxidation pathway in the LR simulation. Right column: the
420 same as the left column but for the relative differences between the RRM and LR simulations. It is noteworthy that
421 the aqueous-phase production occurs in large-scale clouds.

3.4 Aerosol-cloud interactions

423   Aerosol activation in large-scale clouds is parameterized consistently with droplet nucleation. In

424 EAMv1, most IAPs exist in accumulation and Aitken modes (Figures S46a and S46b). We find the

425 aerosol activation in the RRM is, on average, enhanced by 13.7% (accumulation mode) and 5.8% (Aitken

426 mode) compared to the LR (Figures 11a and 11b). Aerosol activation in large-scale clouds primarily

427   occurs in two pathways. One is related to cloud expansion (i.e., increase in cloud fraction, which leads to

428   aerosol activation) and shrinkage (i.e., decrease in cloud fraction, which leads to aerosol resuspension) in

429   the same grid box (hereafter referred to as the cloud-intermittency pathway) between model timesteps.

430   The other refers to the activation of IAPs that are brought to the cloud base by updrafts (hereafter referred

431   to as the updraft pathway) (Liu et al., 2012). We find that the cloud-intermittency pathway contributes to

432   almost all the aerosol activation enhancement in Aitken mode but only about half of the enhancement in

433   accumulation mode under regional refinement (not shown). The updraft pathway accounts for the other

434   half of the enhancement in accumulation mode. The contrast RRM impacts on the updraft pathway

435   between the accumulation and Aitken modes may be related to the distinct vertical profiles of IAPs from

436   the two modes (Figure S46c). The cloud-intermittency pathway is parameterized as a function of W_{sub},

437   aerosol properties, and the change of large-scale liquid cloud fractions between two consecutive time

438   steps (ΔLCLOUD) (Abdul‐Razzak and Ghan, 2000; Zhang et al., 2022a). Positive ΔLCLOUD

439   corresponds to cloud expansion, and negative ΔLCLOUD denotes cloud shrinkage. We do not find any

440   noticeable differences in W_{sub} and aerosol properties between the RRM and LR simulations. However,

441 |ΔLCLOUD| is considerably larger in the RRM, which indicates larger LCLOUD temporal variability

442   (Figure 11c), resulting in increased microphysical cloud processing of aerosols and more aerosol

443   activation via the cloud-intermittency pathway. The larger LCLOUD temporal variability is consistent

444   with the larger relative humidity (RH) temporal variability in the RRM than in the LR (Figure 11d)

445   (Golaz et al., 2002).
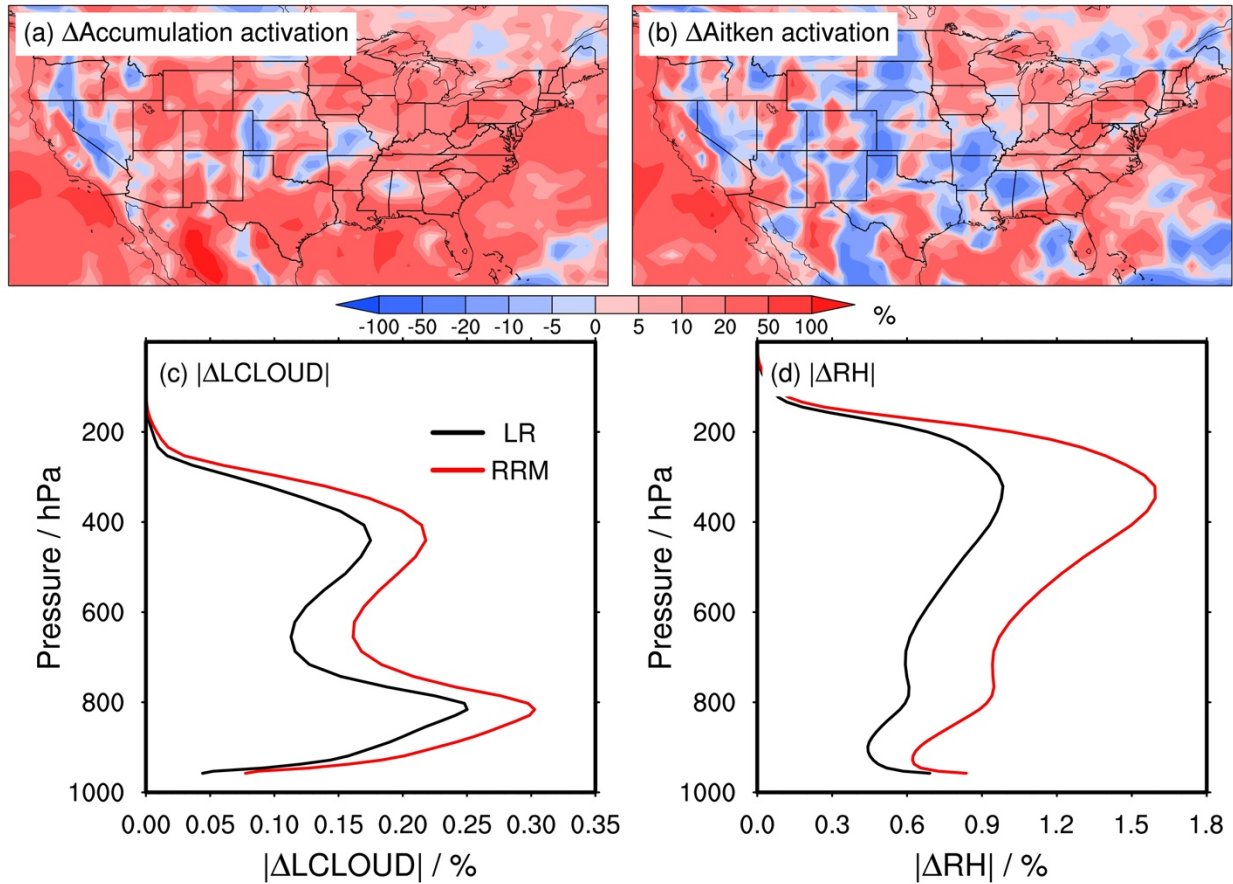
Figure 11. (a, b) Spatial distributions of the relative differences in the annual mean vertical-integrated IAP activation fluxes in large-scale clouds for (a) accumulation and (b) Aitken modes between the RRM and LR simulations. (c) Vertical profiles of the annual regional mean absolute temporal variabilities of large-scale liquid cloud fractions ($|\Delta LCLOUD|$). $|\Delta LCLOUD| = \left| LCLOUD_{t_2} - LCLOUD_{t_1} \right|$; t_2 and t_1 indicate two consecutive model time steps. The red line indicates the RRM simulation and the black line for the LR simulation. (d) the same as (c) but for relative humidity (RH).

Enhanced aerosol activation results in higher droplet number concentrations (N_d) in the RRM compared to the LR (Figure 12a). Moreover, the CLUBB vertical-integrated cloud liquid water tendency (RCMTEND), which is dominated by water vapor condensation, is generally remarkably larger in the RRM simulation (Figure 12b), which leads to higher large-scale cloud liquid water path (LWP) and LWC (Figures 12c and S35c). Larger RCMTEND may also contribute to larger droplets at the cloud top in the RRM simulation (R_e in Figure 12d; R_e — grid-cell mean droplet effective radius at the top of liquid water clouds), even though N_d increases. With higher LWP and larger R_e, cloud optical depth (COD) is also higher (Figure 12e).
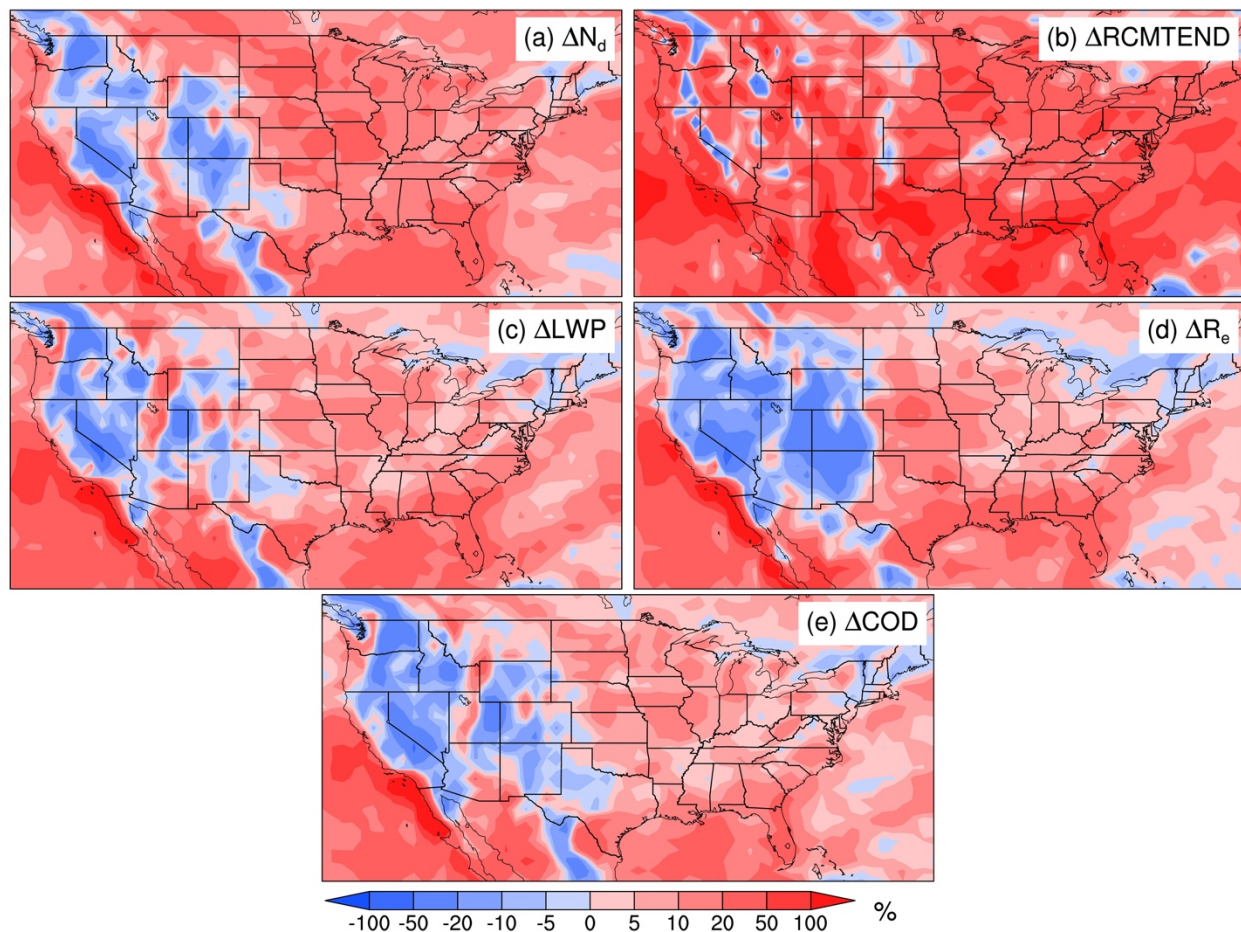
461
462 Figure 12. Spatial distributions of the relative differences in annual mean (a) grid-cell mean vertical-integrated
463 droplet number concentrations (N_d), (b) CLUBB vertical-integrated cloud liquid water tendency (RCMTEND), (c)
464 grid-cell mean liquid water path (LWP), (d) grid-cell mean droplet effective radius at the top of liquid water clouds
465 (R_e), and (e) grid-cell mean cloud optical path (COD) between the RRM and LR simulations. It is noteworthy that
466 N_d, RCMTEND, LWP, and R_e are exclusively for large-scale clouds, while COD considers both large-scale and
467 convective clouds but is dominated by large-scale clouds (not shown). The spatial distributions of N_d, RCMTEND,
468 LWP, R_e, and COD from the LR simulation are shown in Figure S~~5~~7.

3.5 Anthropogenic aerosol effective radiative forcing

470   With considerable impacts on cloud properties, the regional refinement should also influence ERF_{aer}.

471 We use the Ghan (2013) method to decompose ERF_{aer} into direct, indirect, and surface albedo effects.

472 Figure 13 shows a stronger (more negative) anthropogenic aerosol shortwave indirect effect (-0.52 W m^{-2})

473 and enhanced longwave indirect effect (0.21 W m^{-2}) at the top of the model (TOM) in the RRM

474 simulation compared to the LR simulation. The net (shortwave + longwave) indirect effect is 0.31 W m^{-2}

475 more negative in the RRM simulation compared to the LR simulation, which is about a 12%

476 enhancement. The total ERF$_{aer}$ at TOM is 0.27 W m^{-2} more negative in the RRM simulation, about a 12%

477 enhancement compared to the LR simulation. We also find that the RRM simulation produces a 10%

478 enhancement of ERF$_{aer}$ at the surface (Figure S6~~8~~).
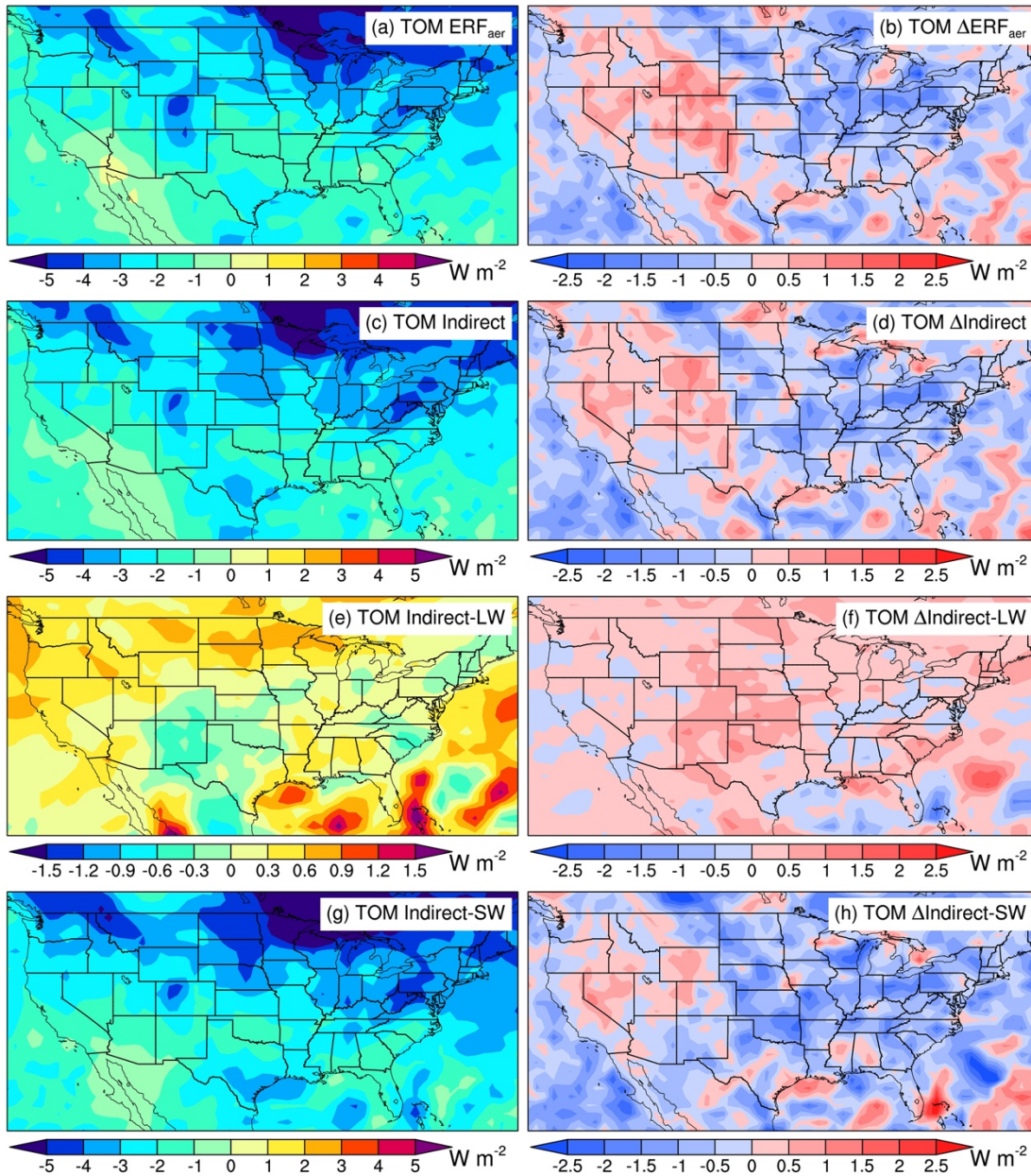
479
480 Figure 13. (a) Spatial distribution of annual mean ERF$_{aer}$ at the top of the model (TOM) from the LR simulation. (c,
481 e, g) Same as (a) but for ERF$_{aer}$ attributed to (c) aerosol indirect effect (longwave + shortwave), (e) aerosol
482 longwave indirect effect, and (g) aerosol shortwave indirect effect. The right column is the same as the left but for
483 the absolute differences between the RRM and LR simulations.

484   To understand the enhancement of ERF_{aer} in the RRM experiment, we compare the production

485   efficiencies of N_d, R_e, LWP, and COD due to anthropogenic aerosols between the RRM and LR

486   simulations (Figure 14). In Figure 14, the relative changes of N_d, LWP, and COD per relative change of

487   CCN at 0.1% supersaturation ($CCN_{0.1\%}$) between the PD and PI simulations are generally larger in the

488   RRM simulation, consistent with our earlier analysis of the enhanced aerosol activation in RRM. Because

489   cloud properties are more sensitive to anthropogenic aerosols in the RRM, the RRM configuration

490   produces stronger anthropogenic-aerosol-cloud interactions and ERF_{aer} (Figure 13).

491   This result differs from Ma et al. (2015), which demonstrated that higher model resolutions would

492   weaken the aerosol indirect effect. Ma et al. (2015) identified the increased droplet nucleation in

493   simulations with higher resolutions, leading to a stronger first aerosol indirect effect, which is consistent

494   with this study. However, their LWP response to anthropogenic aerosols weakens (lower LWP) as

495   resolution increases, leading to reduced second aerosol indirect effect, in contrast to the larger LWP

496   production efficiencies in our RRM simulation (Figure 14b). The discrepancies may be caused by

497   different parameterizations of water vapor condensation to form cloud liquid water. The water vapor

498   condensation is parameterized in CLUBB on the basis of joint PDFs of vertical velocity, temperature, and

499   moisture in our simulations (Golaz et al., 2002), while it was calculated in CAM5 in Ma et al. (2015)

500   using a saturation equilibrium adjustment approach (Park et al., 2014). The water vapor condensation

501   parameterization affects not only LWP but also the subsequent aqueous-phase chemistry calculation

502   discussed in Section 3.3. Therefore, it is necessary to evaluate the sensitivity of water vapor condensation

503   to model resolutions when different parametrizations are used, as their resolution sensitivity can be very

504   different.

505   Our finding regarding the stronger aerosol indirect effect as resolution increases is also different

506   from Caldwell et al. (2019), which found that the aerosol indirect effect changed only slightly from the

507   low-resolution to high-resolution simulations. This discrepancy might be attributed to the fact that the

508   model timesteps used in low- and high-resolution model simulations are very different in Caldwell et al.

509 (2019) but are kept the same in this study. Since model timestep can affect model aerosol and clouds,

510 aerosol indirect effects can be affected.
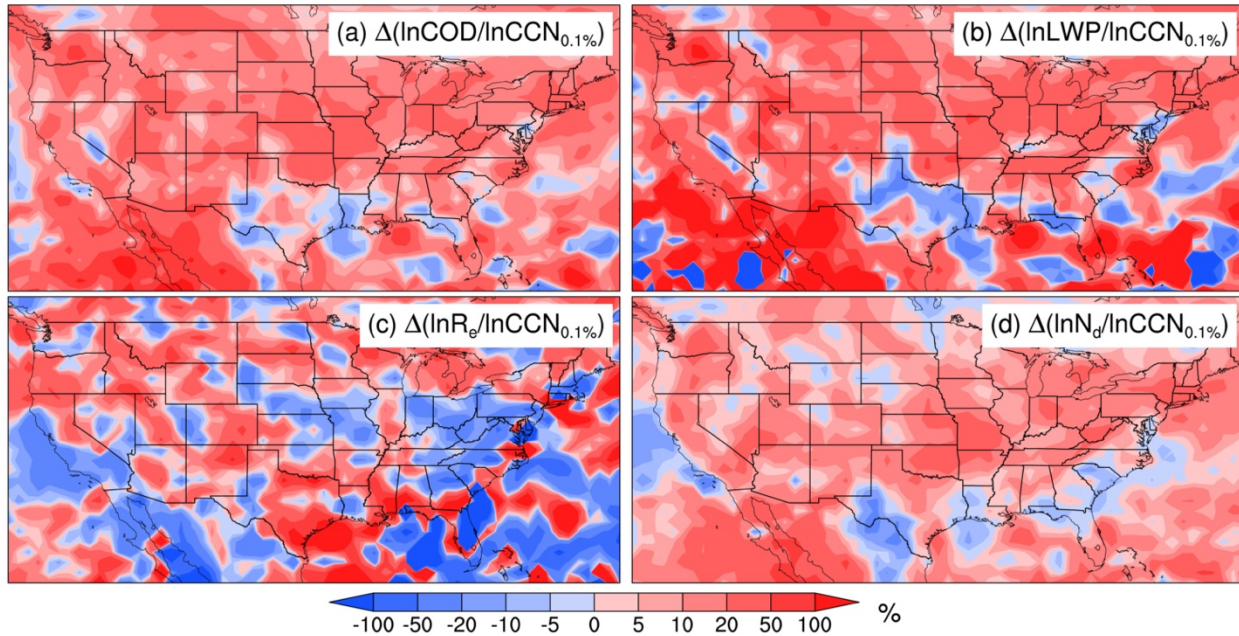
511
512 Figure 14. Spatial distributions of the relative differences in (a) $\frac{\ln COD}{\ln CCN_{0.1\%}}$, (b) $\frac{\ln LWP}{\ln CCN_{0.1\%}}$, (c) $\frac{\ln R_e}{\ln CCN_{0.1\%}}$, and (d)

513 $\frac{\ln N_d}{\ln CCN_{0.1\%}}$ between the RRM and LR simulations. Here, $\ln x$ denotes the relative change of x between the PD and PI

514 simulations, i.e., $\ln x = \frac{PD_x - PI_x}{PI_x}$. Therefore, $\frac{\ln x}{\ln CCN_{0.1\%}}$ reflects the production efficiency of x by anthropogenic

515 aerosols.

4 Conclusions

517   We investigate the impact of increasing model horizontal resolution on the aerosol mass budget and

518 ERF$_{aer}$ over the CONUS in 2016 by comparing E3SMv1 LR and RRM simulations (Tables 1 and 2). The

519 RRM simulation produces more dust, sea salt, and MOM emissions than the LR simulation due to larger

520 surface wind speeds, more frequent strong surface winds, or drier soil. Besides influencing the natural

521 aerosol sources, RRM also affects SO_4 production from gas-aerosol exchange, aqueous-phase chemistry,

522 and NPF (Table 2). The reduced SO_4 production from gas-aerosol exchange and NPF by RRM is due to

523 decreased gas-phase SO_2 and H_2SO_4 concentrations in the RRM simulation. Enhanced aqueous-phase SO_4

524 production consumes more SO_2 under regional refinement, leading to lower gas-phase SO_2

concentrations. The improved aqueous-phase SO_4 production is attributed to more cloud water uptake of H_2SO_4 and more oxidation of SO_2 by H_2O_2 in large-scale clouds with higher LWC in the RRM simulation. In contrast, the oxidation of SO_2 by O_3 is slightly suppressed due to the lower pH of large-scale clouds in the RRM simulation compared to the LR simulation, which is a consequence of slightly increased gas-phase H_2O_2 concentrations releasing more H^+ through the oxidation of SO_2 by H_2O_2.

Table 2. Comparison of aerosol-relevant properties in the RRM region between the LR and RRM simulations

		RRM	LR	Relative diff[1] / %
Precipitation / mm day^{-1}	Large-scale	1.55	1.21	27.5
	Convective	1.00	1.18	-15.6
SO_4 in-cloud scavenging / TgS yr^{-1}	Large-scale precipitation	0.982	0.856	14.7
	Convective precipitation	0.356	0.424	-15.9
SO_4 production / TgS yr^{-1}	Gas-aerosol exchange	0.515	0.531	-3.0
	Aqueous-phase production	1.13	1.06	6.2
	NPF	0.0182	0.0210	-13.3
Aerosol activation / 10^5 m^{-2} s^{-1}	Aitken mode	10.09	8.87	13.7
	Accumulation mode	2.22	2.09	5.8
N_d / 10^{10} m^{-2}		1.30	1.17	11.5
R_e / µm		1.56	1.45	7.7
LWP / g m^{-2}		33.0	30.7	7.3
COD		5.14	4.86	5.6
TOM ERF$_{aer}$ / W m^{-2}	Indirect shortwave	-3.27	-2.74	19.1
	Indirect longwave	0.50	0.29	72.0
	Total indirect	-2.76	-2.45	12.8
	Total (indirect + direct + albedo)	-2.66	-2.38	11.5

[1]*Relative diff* $= (RRM/LR - 1) \times 100\%$.

Increasing model horizontal resolution affects the partitioning between large-scale and convective precipitation (Table 2). With more resolved large-scale precipitation and less parameterized deep

535 convective precipitation, in-cloud scavenging of aerosols by large-scale (deep convective) precipitation

536 generally increases (decreases) in the RRM simulation compared to the LR simulation.

537   RRM enhances the activation of IAPs in large-scale clouds due to the larger temporal variability of

538 LCLOUD in the RRM simulation compared to the LR simulation (Table 2). Enhanced aerosol activation

539 leads to more cloud droplets. In addition, RRM enhances water vapor condensation, resulting in larger

540 LWP and R_e, which leads to larger COD. Since aerosol activation is stronger in the RRM simulation,

541 cloud droplets, LWP, and COD are more sensitive to anthropogenic aerosols. Consequently, the

542 anthropogenic aerosol indirect effect and ERF_{aer} in the RRM are stronger than in the LR simulation (Table

543 2).

544   Although the study is limited to comparing the E3SMv1 LR (~100 km) and CONUS RRM (~25 km)

545 simulations, the methodology shown in the study is helpful for future studies to investigate the potential

546 impacts of model resolutions on the simulation results, as RRM is significantly less expensive

547 computationally compared to the global high-resolution model. ~~And some~~Some findings from this study

548 may also apply to E3SM simulations at higher resolutions or even convection-permitting scales, such as

549 the enhancement in natural aerosol emissions due to stronger winds, the partitioning between large-scale

550 and convective precipitation and associated wet scavenging, and improved IAP activation in large-scale

551 clouds. However, we must also emphasize that the aerosol mass budget and ERF_{aer} are sensitive to model

552 configurations and regional characteristics such as aerosol properties, land use and land cover, and

553 climate. Aerosol and clouds in other regions can be very different. Furthermore, some resolution

554 sensitivities may differ as model resolution advances to convection-permitting and subgrid-scale

555 processes ~~becomes~~become more significant. Moreover, although nudging is applied in the study to

556 minimize the impacts of large-scale circulations on aerosol properties as horizontal resolution changes,

557 differences in meteorology still exist between the RRM and LR simulations (e.g., surface wind speed and

558 precipitation). Therefore, the results above contain the meteorological effect, although the meteorological

559 differences are also caused by the change in horizontal grid spacing.

560

Code availability

The E3SMv1 source code is available at https://doi.org/10.11578/E3SM/dc.20180418.36 (E3SM Project, 2018) (last access: April 11, 2022).

Data availability

We use the Stage IV precipitation data from the MCS-IDC data product, available at http://dx.doi.org/10.25584/1632005 (Li et al., 2020). The LR and RRM simulation results are available at https://doi.org/10.5281/zenodo.7782985 (Li et al., 2023). The level-3 Moderate Resolution Imaging Spectroradiometer (MODIS) gridded (1° × 1°) monthly Dark Target aerosol optical depth (AOD) products used in the supplement are from https://doi.org/10.5067/MODIS/MOD08_M3.061 (MOD08_M3; last access: Nov 28, 2023) and https://doi.org/10.5067/MODIS/MYD08_M3.061 (MYD08_M3; last access: Nov 28, 2023). The Aerosol Robotic Network (AERONET) data is available at https://aeronet.gsfc.nasa.gov/new_web/download_all_v3_aod.html (last access: May 26, 2022). The Interagency Monitoring of Protected Visual Environments (IMPROVE) data is available at https://views.cira.colostate.edu/fed/QueryWizard/ (last access: May 26, 2022).

Author contributions

KZ and JL designed the study. JL conducted the simulations under the instructions of KZ and with the help of TH, BS, and QY. KZ and SZ determined the nudging strategy, and JL prepared the ERA5 nudging files under the instructions of SZ and KZ. JL performed the analyses with discussions with KZ, TH, PM, and HH. JL prepared the paper with contributions from all coauthors.

Competing Interests

Po-Lun Ma is a Topical Editor of Geoscientific Model Development. Other authors declare that they have no conflict of interest.

Acknowledgments

The study was supported as part of the Enabling Aerosol–cloud interactions at GLobal convection-permitting scalES (EAGLES) project (project no. 74358) sponsored by the United States Department of Energy (DOE), Office of Science, Office of Biological and Environmental Research, Earth System Model Development (ESMD) program area. The Pacific Northwest National Laboratory (PNNL) is operated for the DOE by the Battelle Memorial Institute under Contract DE-AC05-76RL01830. The research used high-performance computing resources from the PNNL Research Computing and resources of the National Energy Research Scientific Computing Center (NERSC), a U.S. Department of Energy Office of Science User Facility located at Lawrence Berkeley National Laboratory, operated under Contract No. DE-AC02-05CH11231 using NERSC awards ALCC-ERCAP0016315, BER-ERCAP0015329, BER-ERCAP0018473, and BER-ERCAP0020990. IMPROVE is a collaborative association of state, tribal, and federal agencies, and international partners. US Environmental Protection Agency is the primary funding source, with contracting and research support from the National Park Service. The Air Quality Group at the University of California, Davis is the central analytical laboratory, with ion analysis provided by Research Triangle Institute, and carbon analysis provided by Desert Research Institute. We thank Ilya Slutsker and many other Principal Investigators (PIs) or co-PIs and their staff for establishing and maintaining the AERONET sites used in the study.

References

Abdul‑Razzak, H., and Ghan, S. J.: A parameterization of aerosol activation: 2. Multiple aerosol types, J. Geophys. Res.-Atmos., 105, 6837-6844, https://doi.org/10.1029/1999JD901161, 2000.

Apte, J. S., Marshall, J. D., Cohen, A. J., and Brauer, M.: Addressing global mortality from ambient $PM_{2.5}$, Environ. Sci. Technol., 49, 8057-8066, https://doi.org/10.1021/acs.est.5b01236, 2015.

Barth, M., Rasch, P., Kiehl, J., Benkovitz, C., and Schwartz, S.: Sulfur chemistry in the National Center for Atmospheric Research Community Climate Model: Description, evaluation, features, and sensitivity to aqueous chemistry, J. Geophys. Res.-Atmos., 105, 1387-1415, https://doi.org/10.1029/1999JD900773, 2000.

Bogenschutz, P. A., Gettelman, A., Morrison, H., Larson, V. E., Craig, C., and Schanen, D. P.: Higher-order turbulence closure and its impact on climate simulations in the Community Atmosphere Model, J. Clim., 26, 9655-9676, https://doi.org/10.1175/JCLI-D-13-00075.1, 2013.

Burrows, S. M., Easter, R. C., Liu, X., Ma, P.-L., Wang, H., Elliott, S. M., Singh, B., Zhang, K., and Rasch, P. J.: OCEANFILMS (Organic Compounds from Ecosystems to Aerosols: Natural Films and Interfaces via Langmuir Molecular Surfactants) sea spray organic aerosol emissions–implementation in a global climate model and impacts on clouds, Atmos. Chem. Phys., 22, 5223-5251, https://doi.org/10.5194/acp-22-5223-2022, 2022.

Caldwell, P. M., Mametjanov, A., Tang, Q., Van Roekel, L. P., Golaz, J. C., Lin, W., Bader, D. C., Keen, N. D., Feng, Y., and Jacob, R.: The DOE E3SM coupled model version 1: Description and results at high resolution, Journal of Advances in Modeling Earth Systems, 11, 4095-4146, https://doi.org/10.1029/2019MS001870, 2019.

Caldwell, P. M., Terai, C. R., Hillman, B., Keen, N. D., Bogenschutz, P., Lin, W., Beydoun, H., Taylor, M., Bertagna, L., and Bradley, A.: Convection‑permitting simulations with the E3SM global atmosphere model, Journal of Advances in Modeling Earth Systems, 13, e2021MS002544, https://doi.org/10.1029/2021MS002544, 2021.

Dennis, J. M., Edwards, J., Evans, K. J., Guba, O., Lauritzen, P. H., Mirin, A. A., St-Cyr, A., Taylor, M. A., and Worley, P. H.: CAM-SE: A scalable spectral element dynamical core for the Community Atmosphere Model, The International Journal of High Performance Computing Applications, 26, 74-89, https://doi.org/10.1177/1094342011428142, 2012.

Dueben, P. D., Wedi, N., Saarinen, S., and Zeman, C.: Global simulations of the atmosphere at 1.45 km grid-spacing with the Integrated Forecasting System, Journal of the Meteorological Society of Japan. Ser. II, 98, 551-572, https://doi.org/10.2151/jmsj.2020-016, 2020.

E3SM Project, DOE: Energy Exascale Earth System Model v1.0, [code], https://doi.org/10.11578/E3SM/dc.20180418.36, 2018.

Feng, L., Smith, S. J., Braun, C., Crippa, M., Gidden, M. J., Hoesly, R., Klimont, Z., Van Marle, M., Van Den Berg, M., and Van Der Werf, G. R.: The generation of gridded emissions data for CMIP6, Geoscientific Model Development, 13, 461-482, https://doi.org/10.5194/gmd-13-461-2020, 2020.

Feng, Y., Wang, H., Rasch, P., Zhang, K., Lin, W., Tang, Q., Xie, S., Hamilton, D., Mahowald, N., and Yu, H.: Global dust cycle and direct radiative effect in E3SM version 1: Impact of increasing model resolution, Journal of Advances in Modeling Earth Systems, 14, e2021MS002909, https://doi.org/10.1029/2021MS002909, 2022.

641 Feng, Z., Song, F., Sakaguchi, K., and Leung, L. R.: Evaluation of Mesoscale Convective Systems in Climate
642 Simulations: Methodological Development and Results from MPAS-CAM over the United States, J. Clim., 34,
643 2611-2633, https://doi.org/10.1175/JCLI-D-20-0136.1, 2021.

644 Ghan, S. J.: Estimating aerosol effects on cloud radiative forcing, Atmos. Chem. Phys., 13, 9971-9974,
645 https://doi.org/10.5194/acp-13-9971-2013, 2013.

646 Golaz, J.-C., Larson, V. E., and Cotton, W. R.: A PDF-based model for boundary layer clouds. Part I: Method and
647 model description, Journal of the atmospheric sciences, 59, 3540-3551, https://doi.org/10.1175/1520-
648 0469(2002)059<3540:APBMFB>2.0.CO;2, 2002.

649 Golaz, J.-C., Van Roekel, L. P., Zheng, X., Roberts, A. F., Wolfe, J. D., Lin, W., Bradley, A. M., Tang, Q., Maltrud,
650 M. E., and Forsyth, R. M.: The DOE E3SM Model Version 2: overview of the physical model and initial model
651 evaluation, Journal of Advances in Modeling Earth Systems, 14, https://doi.org/10.1029/2022MS003156, 2022.

652 Golaz, J. C., Caldwell, P. M., Van Roekel, L. P., Petersen, M. R., Tang, Q., Wolfe, J. D., Abeshu, G., Anantharaj,
653 V., Asay‑Davis, X. S., and Bader, D. C.: The DOE E3SM coupled model version 1: Overview and evaluation at
654 standard resolution, Journal of Advances in Modeling Earth Systems, 11, 2089-2129,
655 https://doi.org/10.1029/2018MS001603, 2019.

656 Hamilton, D. S., Perron, M. M., Bond, T. C., Bowie, A. R., Buchholz, R. R., Guieu, C., Ito, A., Maenhaut, W.,
657 Myriokefalitakis, S., and Olgun, N.: Earth, wind, fire, and pollution: Aerosol nutrient sources and impacts on ocean
658 biogeochemistry, Annual Review of Marine Science, 14, 303-330, https://doi.org/10.1146/annurev-marine-031921-
659 013612, 2022.

660 Harris, L. M., Lin, S.-J., and Tu, C.: High-resolution climate simulations using GFDL HiRAM with a stretched
661 global grid, J. Clim., 29, 4293-4314, https://doi.org/10.1175/JCLI-D-15-0389.1, 2016.

662 Heinzeller, D., Duda, M. G., and Kunstmann, H.: Towards convection-resolving, global atmospheric simulations
663 with the Model for Prediction Across Scales (MPAS) v3.1: An extreme scaling experiment, Geoscientific Model
664 Development, 9, 77-110, https://doi.org/10.5194/gmd-9-77-2016, 2016.

665 Hersbach, H., Bell, B., Berrisford, P., Hirahara, S., Horányi, A., Muñoz‑Sabater, J., Nicolas, J., Peubey, C., Radu,
666 R., and Schepers, D.: The ERA5 global reanalysis, Quarterly Journal of the Royal Meteorological Society, 146,
667 1999-2049, https://doi.org/10.1002/qj.3803, 2020.

668 Hoesly, R. M., Smith, S. J., Feng, L., Klimont, Z., Janssens-Maenhout, G., Pitkanen, T., Seibert, J. J., Vu, L.,
669 Andres, R. J., and Bolt, R. M.: Historical (1750–2014) anthropogenic emissions of reactive gases and aerosols from
670 the Community Emissions Data System (CEDS), Geoscientific Model Development, 11, 369-408,
671 https://doi.org/10.5194/gmd-11-369-2018, 2018.

672 Hoose, C., Kristjánsson, J. E., Chen, J.-P., and Hazra, A.: A classical-theory-based parameterization of
673 heterogeneous ice nucleation by mineral dust, soot, and biological particles in a global climate model, Journal of the
674 Atmospheric Sciences, 67, 2483-2503, https://doi.org/10.1175/2010JAS3425.1, 2010.

675 Hurrell, J. W., Hack, J. J., Shea, D., Caron, J. M., and Rosinski, J.: A new sea surface temperature and sea ice
676 boundary dataset for the Community Atmosphere Model, J. Clim., 21, 5145-5153,
677 https://doi.org/10.1175/2008JCLI2292.1, 2008.

678 Iacono, M. J., Delamere, J. S., Mlawer, E. J., Shephard, M. W., Clough, S. A., and Collins, W. D.: Radiative forcing
679 by long‑lived greenhouse gases: Calculations with the AER radiative transfer models, J. Geophys. Res.-Atmos.,
680 113, https://doi.org/10.1029/2008JD009944, 2008.

Jickells, T., An, Z., Andersen, K. K., Baker, A., Bergametti, G., Brooks, N., Cao, J., Boyd, P., Duce, R., and Hunter, K.: Global iron connections between desert dust, ocean biogeochemistry, and climate, Science, 308, 67-71, https://doi.org/10.1126/science.1105959, 2005.

Kooperman, G. J., Pritchard, M. S., Ghan, S. J., Wang, M., Somerville, R. C., and Russell, L. M.: Constraining the influence of natural variability to improve estimates of global aerosol indirect effects in a nudged version of the Community Atmosphere Model 5, J. Geophys. Res.-Atmos., 117, https://doi.org/10.1029/2012JD018588, 2012.

Larson, V. E., Golaz, J.-C., and Cotton, W. R.: Small-scale and mesoscale variability in cloudy boundary layers: Joint probability density functions, Journal of the atmospheric sciences, 59, 3519-3539, https://doi.org/10.1175/1520-0469(2002)059<3519:SSAMVI>2.0.CO;2, 2002.

Li, J., Han, X., Jin, M., Zhang, X., and Wang, S.: Globally analysing spatiotemporal trends of anthropogenic $PM_{2.5}$ concentration and population's $PM_{2.5}$ exposure from 1998 to 2016, Environ. Int., 128, 46-62, https://doi.org/10.1016/j.envint.2019.04.026, 2019.

Li, J., Feng, Z., Qian, Y., and Leung, L. R.: MCSs and IDC in the US for 2004 – 2017, http://dx.doi.org/10.25584/1632005, 2020 (last access: June 18, 2020).

Li, J., Feng, Z., Qian, Y., and Leung, L. R.: A high-resolution unified observational data product of mesoscale convective systems and isolated deep convection in the United States for 2004–2017, Earth Syst. Sci. Data, 13, 827-856, https://doi.org/10.5194/essd-13-827-2021, 2021.

Li, J., Zhang, K., Hassan, T., Zhang, S., Ma, P.-L., Singh, B., Yan, Q., and Huang, H.: Assessing the Sensitivity of Aerosol Mass Budget and Effective Radiative Forcing to Horizontal Grid Spacing in E3SMv1 Using A Regional Refinement Approach - E3SM LR and RRM simulation data, https://doi.org/10.5281/zenodo.7782985, 2023 (last access: March 29, 2023).

Lim, C.-H., Ryu, J., Choi, Y., Jeon, S. W., and Lee, W.-K.: Understanding global PM2.5 concentrations and their drivers in recent decades (1998–2016), Environ. Int., 144, 106011, https://doi.org/10.1016/j.envint.2020.106011, 2020.

Lin, Y., and Mitchell, K. E.: the NCEP stage II/IV hourly precipitation analyses: Development and applications, 19th Conf. Hydrology, American Meteorological Society, San Diego, CA, USA, 2005,

Liu, X., Easter, R. C., Ghan, S. J., Zaveri, R., Rasch, P., Shi, X., Lamarque, J.-F., Gettelman, A., Morrison, H., and Vitt, F.: Toward a minimal representation of aerosols in climate models: Description and evaluation in the Community Atmosphere Model CAM5, Geoscientific Model Development, 5, 709-739, https://doi.org/10.5194/gmd-5-709-2012, 2012.

Liu, X., Ma, P. L., Wang, H., Tilmes, S., Singh, B., Easter, R. C., Ghan, S. J., and Rasch, P. J.: Description and evaluation of a new four-mode version of the Modal Aerosol Module (MAM4) within version 5.3 of the Community Atmosphere Model, Geosci. Model Dev., 9, 505-522, https://doi.org/10.5194/gmd-9-505-2016, 2016.

Ma, P.-L., Rasch, P. J., Fast, J. D., Easter, R. C., Gustafson Jr, W., Liu, X., Ghan, S. J., and Singh, B.: Assessing the CAM5 physics suite in the WRF-Chem model: Implementation, resolution sensitivity, and a first evaluation for a regional case study, Geoscientific Model Development, 7, 755-778, https://doi.org/10.5194/gmd-7-755-2014, 2014.

Ma, P. L., Rasch, P. J., Wang, M., Wang, H., Ghan, S. J., Easter, R. C., Gustafson Jr, W. I., Liu, X., Zhang, Y., and Ma, H. Y.: How does increasing horizontal resolution in a global climate model improve the simulation of aerosol‐cloud interactions?, Geophys. Res. Lett., 42, 5058-5065, https://doi.org/10.1002/2015GL064183, 2015.

Mahowald, N. M., Scanza, R., Brahney, J., Goodale, C. L., Hess, P. G., Moore, J. K., and Neff, J.: Aerosol deposition impacts on land and ocean carbon cycles, Current Climate Change Reports, 3, 16-31, https://doi.org/10.1007/s40641-017-0056-z, 2017.

Mlawer, E. J., Taubman, S. J., Brown, P. D., Iacono, M. J., and Clough, S. A.: Radiative transfer for inhomogeneous atmospheres: RRTM, a validated correlated‐k model for the longwave, J. Geophys. Res.-Atmos., 102, 16663-16682, https://doi.org/10.1029/97JD00237, 1997.

Morrison, H., and Gettelman, A.: A new two-moment bulk stratiform cloud microphysics scheme in the Community Atmosphere Model, version 3 (CAM3). Part I: Description and numerical tests, J. Clim., 21, 3642-3659, https://doi.org/10.1175/2008JCLI2105.1, 2008.

Namikas, S., and Sherman, D. J.: Predicting aeolian sand transport: Revisiting the White model, Earth Surface Processes and Landforms: The Journal of the British Geomorphological Group, 22, 601-604, https://doi.org/10.1002/(SICI)1096-9837(199706)22:6<601::AID-ESP783>3.0.CO;2-5, 1997.

Neale, R. B., Richter, J. H., and Jochum, M.: The impact of convection on ENSO: From a delayed oscillator to a series of events, J. Clim., 21, 5904-5924, https://doi.org/10.1175/2008JCLI2244.1, 2008.

Oleson, K. W., Lawrence, D. M., Bonan, G. B., Drewniak, B., Huang, M., Koven, C. D., Levis, S., Li, F., Riley, W. J., Subin, Z. M., Swenson, S. C., Thornton, P. E., Bozbiyik, A., Fisher, R., Heald, C. L., Kluzek, E., Lamarque, J.-F., Lawrence, P. J., Leung, L. R., Lipscomb, W., Muszala, S., Ricciuto, D. M., Sacks, W., Sun, Y., Tang, J., and Yang, Z.-L.: Technical Description of version 4.5 of the Community Land Model (CLM), available at http://dx.doi.org/10.5065/D6RR1W7M, National Center for Atmospheric Research, Boulder, Colorado, US, 434, 2013.

Park, S., Bretherton, C. S., and Rasch, P. J.: Integrating cloud processes in the Community Atmosphere Model, version 5, J. Clim., 27, 6821-6856, https://doi.org/10.1175/JCLI-D-14-00087.1, 2014.

Perring, A., Pusede, S., and Cohen, R.: An observational perspective on the atmospheric impacts of alkyl and multifunctional nitrates on ozone and secondary organic aerosol, Chem. Rev., 113, 5848-5870, https://doi.org/10.1021/cr300520x, 2013.

Pusede, S. E., Steiner, A. L., and Cohen, R. C.: Temperature and recent trends in the chemistry of continental surface ozone, Chem. Rev., 115, 3898-3918, https://doi.org/10.1021/cr5006815, 2015.

Qian, Y., Yasunari, T. J., Doherty, S. J., Flanner, M. G., Lau, W. K., Ming, J., Wang, H., Wang, M., Warren, S. G., and Zhang, R.: Light-absorbing particles in snow and ice: Measurement and modeling of climatic and hydrological impact, Advances in Atmospheric Sciences, 32, 64-91, https://doi.org/10.1007/s00376-014-0010-0, 2015.

Rasch, P., Feichter, J., Law, K., Mahowald, N., Penner, J., Benkovitz, C., Genthon, C., Giannakopoulos, C., Kasibhatla, P., and Koch, D.: A comparison of scavenging and deposition processes in global models: results from the WCRP Cambridge Workshop of 1995, Tellus B, 52, 1025-1056, https://doi.org/10.1034/j.1600-0889.2000.00980.x, 2000.

Rasch, P., Xie, S., Ma, P. L., Lin, W., Wang, H., Tang, Q., Burrows, S., Caldwell, P., Zhang, K., and Easter, R.: An overview of the atmospheric component of the Energy Exascale Earth System Model, Journal of Advances in Modeling Earth Systems, 11, 2377-2411, https://doi.org/10.1029/2019MS001629, 2019.

Ridley, D. A., Heald, C. L., Pierce, J., and Evans, M.: Toward resolution‐independent dust emissions in global models: Impacts on the seasonal and spatial distribution of dust, Geophys. Res. Lett., 40, 2873-2877, https://doi.org/10.1002/grl.50409, 2013.

760 Schwartz, C. S.: Medium-range convection-allowing ensemble forecasts with a variable-resolution global model,
761 Monthly Weather Review, 147, 2997-3023, https://doi.org/10.1175/MWR-D-18-0452.1, 2019.

762 Seinfeld, J. H., and Pandis, S. N.: Atmospheric chemistry and physics: from air pollution to climate change, John
763 Wiley & Sons, Inc, Hoboken, New Jersey, 2016.

764 Shrivastava, M., Easter, R. C., Liu, X., Zelenyuk, A., Singh, B., Zhang, K., Ma, P. L., Chand, D., Ghan, S., and
765 Jimenez, J. L.: Global transformation and fate of SOA: Implications of low‐volatility SOA and gas‐phase
766 fragmentation reactions, J. Geophys. Res.-Atmos., 120, 4169-4195, https://doi.org/10.1002/2014JD022563, 2015.

767 Smith, C. J., Kramer, R. J., Myhre, G., Alterskjær, K., Collins, W., Sima, A., Boucher, O., Dufresne, J.-L., Nabat,
768 P., and Michou, M.: Effective radiative forcing and adjustments in CMIP6 models, Atmos. Chem. Phys., 20, 9591-
769 9618, https://doi.org/10.5194/acp-20-9591-2020, 2020.

770 Sun, J., Zhang, K., Wan, H., Ma, P. L., Tang, Q., and Zhang, S.: Impact of nudging strategy on the climate
771 representativeness and hindcast skill of constrained EAMv1 simulations, Journal of Advances in Modeling Earth
772 Systems, 11, 3911-3933, https://doi.org/10.1029/2019MS001831, 2019.

773 Tang, Q., Klein, S. A., Xie, S., Lin, W., Golaz, J. C., Roesler, E. L., Taylor, M. A., Rasch, P. J., Bader, D. C., Berg,
774 L. K., Caldwell, P., Giangrande, S. E., Neale, R. B., Qian, Y., Riihimaki, L. D., Zender, C. S., Zhang, Y., and
775 Zheng, X.: Regionally refined test bed in E3SM atmosphere model version 1 (EAMv1) and applications for high-
776 resolution modeling, Geosci. Model Dev., 12, 2679-2706, https://doi.org/10.5194/gmd-12-2679-2019, 2019.

777 Van Marle, M. J., Kloster, S., Magi, B. I., Marlon, J. R., Daniau, A.-L., Field, R. D., Arneth, A., Forrest, M.,
778 Hantson, S., and Kehrwald, N. M.: Historic global biomass burning emissions for CMIP6 (BB4CMIP) based on
779 merging satellite observations with proxies and fire models (1750–2015), Geoscientific Model Development, 10,
780 3329-3357, https://doi.org/10.5194/gmd-10-3329-2017, 2017.

781 Wan, H., Rasch, P. J., Taylor, M. A., and Jablonowski, C.: Short‐term time step convergence in a climate model,
782 Journal of advances in modeling earth systems, 7, 215-225, https://doi.org/10.1002/2014MS000368, 2015.

783 Wan, H., Zhang, S., Rasch, P. J., Larson, V. E., Zeng, X., and Yan, H.: Quantifying and attributing time step
784 sensitivities in present-day climate simulations conducted with EAMv1, Geoscientific Model Development, 14,
785 1921-1948, https://doi.org/10.5194/gmd-14-1921-2021, 2021.

786 Wang, H., Easter, R. C., Rasch, P. J., Wang, M., Liu, X., Ghan, S. J., Qian, Y., Yoon, J.-H., Ma, P.-L., and Vinoj,
787 V.: Sensitivity of remote aerosol distributions to representation of cloud–aerosol interactions in a global climate
788 model, Geoscientific Model Development, 6, 765-782, https://doi.org/10.5194/gmd-6-765-2013, 2013.

789 Wang, H., Easter, R. C., Zhang, R., Ma, P. L., Singh, B., Zhang, K., Ganguly, D., Rasch, P. J., Burrows, S. M., and
790 Ghan, S. J.: Aerosols in the E3SM Version 1: New developments and their impacts on radiative forcing, Journal of
791 Advances in Modeling Earth Systems, 12, e2019MS001851, https://doi.org/10.1029/2019MS001851, 2020.

792 Wang, J., Fan, J., Feng, Z., Zhang, K., Roesler, E., Hillman, B., Shpund, J., Lin, W., and Xie, S.: Impact of a new
793 cloud microphysics parameterization on the simulations of mesoscale convective systems in E3SM, Journal of
794 Advances in Modeling Earth Systems, 13, e2021MS002628, https://doi.org/10.1029/2021MS002628, 2021.

795 Wang, S., Maltrud, M., Elliott, S., Cameron-Smith, P., and Jonko, A.: Influence of dimethyl sulfide on the carbon
796 cycle and biological production, Biogeochemistry, 138, 49-68, https://doi.org/10.1007/s10533-018-0430-5, 2018.

797 Wang, X., Zhang, R., and Yu, W.: The effects of $PM_{2.5}$ concentrations and relative humidity on atmospheric
798 visibility in Beijing, J. Geophys. Res.-Atmos., 124, 2235-2259, https://doi.org/10.1029/2018JD029269, 2019.

Wang, Y., Liu, X., Hoose, C., and Wang, B.: Different contact angle distributions for heterogeneous ice nucleation in the Community Atmospheric Model version 5, Atmos. Chem. Phys., 14, 10411-10430, https://doi.org/10.5194/acp-14-10411-2014, 2014.

Xiao, Q., Zheng, Y., Geng, G., Chen, C., Huang, X., Che, H., Zhang, X., He, K., and Zhang, Q.: Separating emission and meteorological contributions to long-term $PM_{2.5}$ trends over eastern China during 2000–2018, Atmos. Chem. Phys., 21, 9475-9496, https://doi.org/10.5194/acp-21-9475-2021, 2021.

Xie, S., Lin, W., Rasch, P. J., Ma, P. L., Neale, R., Larson, V. E., Qian, Y., Bogenschutz, P. A., Caldwell, P., and Cameron‑Smith, P.: Understanding cloud and convective characteristics in version 1 of the E3SM atmosphere model, Journal of Advances in Modeling Earth Systems, 10, 2618-2644, https://doi.org/10.1029/2018MS001350, 2018.

Zarzycki, C. M., Levy, M. N., Jablonowski, C., Overfelt, J. R., Taylor, M. A., and Ullrich, P. A.: Aquaplanet experiments using CAM's variable-resolution dynamical core, J. Clim., 27, 5481-5503, https://doi.org/10.1175/JCLI-D-14-00004.1, 2014.

Zender, C. S., Bian, H., and Newman, D.: Mineral Dust Entrainment and Deposition (DEAD) model: Description and 1990s dust climatology, J. Geophys. Res.-Atmos., 108, https://doi.org/10.1029/2002JD002775, 2003.

Zhang, G. J., and McFarlane, N. A.: Sensitivity of climate simulations to the parameterization of cumulus convection in the Canadian Climate Centre general circulation model, Atmosphere-Ocean, 33, 407-446, https://doi.org/10.1080/07055900.1995.9649539, 1995.

Zhang, K., Wan, H., Liu, X., Ghan, S. J., Kooperman, G. J., Ma, P.-L., Rasch, P. J., Neubauer, D., and Lohmann, U.: On the use of nudging for aerosol–climate model intercomparison studies, Atmos. Chem. Phys., 14, 8631-8645, https://doi.org/10.5194/acp-14-8631-2014, 2014.

Zhang, K., Zhang, W., Wan, H., Rasch, P. J., Ghan, S. J., Easter, R. C., Shi, X., Wang, Y., Wang, H., and Ma, P.-L.: Effective radiative forcing of anthropogenic aerosols in E3SM version 1: historical changes, causality, decomposition, and parameterization sensitivities, Atmos. Chem. Phys., 22, 9129-9160, https://doi.org/10.5194/acp-22-9129-2022, 2022a.

Zhang, S., Zhang, K., Wan, H., and Sun, J.: Further improvement and evaluation of nudging in the E3SM Atmosphere Model version 1 (EAMv1): simulations of the mean climate, weather events, and anthropogenic aerosol effects, Geoscientific Model Development, 15, 6787-6816, https://doi.org/10.5194/gmd-15-6787-2022, 2022b.

Zhao, C., Liu, X., Qian, Y., Yoon, J., Hou, Z., Lin, G., McFarlane, S., Wang, H., Yang, B., and Ma, P.-L.: A sensitivity study of radiative fluxes at the top of atmosphere to cloud-microphysics and aerosol parameters in the community atmosphere model CAM5, Atmos. Chem. Phys., 13, 10969-10987, https://doi.org/10.5194/acp-13-10969-2013, 2013.

1 Supplementary information for

Assessing the Sensitivity of Aerosol Mass Budget and

Effective Radiative Forcing to Horizontal Grid Spacing in

E3SMv1 Using A Regional Refinement Approach

5 Jianfeng Li[1, *], Kai Zhang[1, *], Taufiq Hassan[1], Shixuan Zhang[1], Po-Lun Ma[1], Balwinder Singh[1],
6 Qiyang Yan[1, a], Huilin Huang[1]

7 [1]Atmospheric Sciences and Global Change Division, Pacific Northwest National Laboratory,
8 Richland, Washington, US

9 [a]now at KLA Corporation, US

11 * Correspondence to Jianfeng Li (jianfeng.li@pnnl.gov) and Kai Zhang (Kai.Zhang@pnnl.gov)

13   Table S1. Evaluation statistics of aerosol optical depth (AOD) at 550 nm based on Figure S1

	MODIS[1]	LR			RRM		
	Mean[2]	Mean	RMSE	r	Mean	RMSE	r
ANN	0.159	0.130	0.084	0.66	0.130	0.084	0.66
JJA	0.164	0.149	0.098	0.72	0.149	0.099	0.72
DJF	0.162	0.130	0.092	0.68	0.129	0.093	0.68

14   [1]We use the level-3 MODIS (Moderate Resolution Imaging Spectroradiometer) gridded (1° × 1°) monthly Dark
15   Target AOD products (MOD08_M3 and MYD08_M3) in 2016 (Platnick et al., 2015). MOD08_M3 provides
16   monthly mean AOD at 10:30 local solar time (LST), while MYD08_M3 provides monthly mean AOD at 13:30
17   LST. The averages of monthly MOD08_M3 and MYD08_M3 AOD are used to calculate the MODIS annual, JJA
18   (June, July, and August), and DJF (December, January, and February) mean AOD all over the globe in Figure S1,
19   which are then used to derive the statistics here.
20   [2]"Mean" refers to the global mean; RMSE (root-mean-square-error) and r (Pearson correlation coefficient) are
21   against MODIS observations.
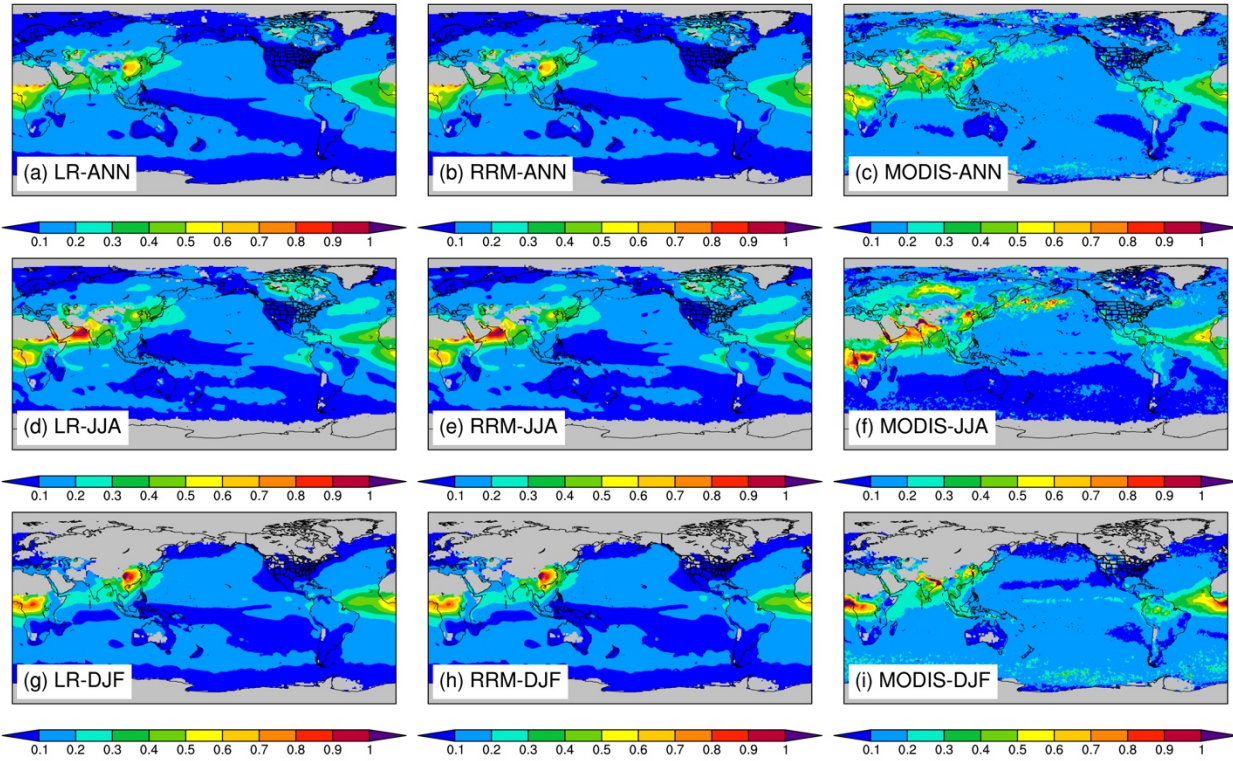
Figure S1. Spatial distributions of AOD at 550 nm from the (a, d, g) LR and (b, e, h) RRM simulations and (c, f, i) the MODIS datasets in 2016. (a, b, c) ANN refers to the annual mean, (d, e, f) JJA indicates the mean AOD during June, July, and August, and (g, h, i) represents the mean during December, January, and February. For the LR and RRM simulations, we output averaged AOD during 10:00-11:00 LST and 13:00-14:00 LST each day to match MOD and MYD observations, respectively. Calculated monthly AOD during the two periods from the LR and RRM simulations are then filtered using the corresponding data availability of MOD08_M3 and MYD08_M3 AOD at 550 nm, which are then used to calculate averaged AOD of the two periods). Finally, we use the monthly averaged AOD to calculate the annual, JJA, and DJF mean AOD for the LR and RRM simulations and the MODIS datasets.
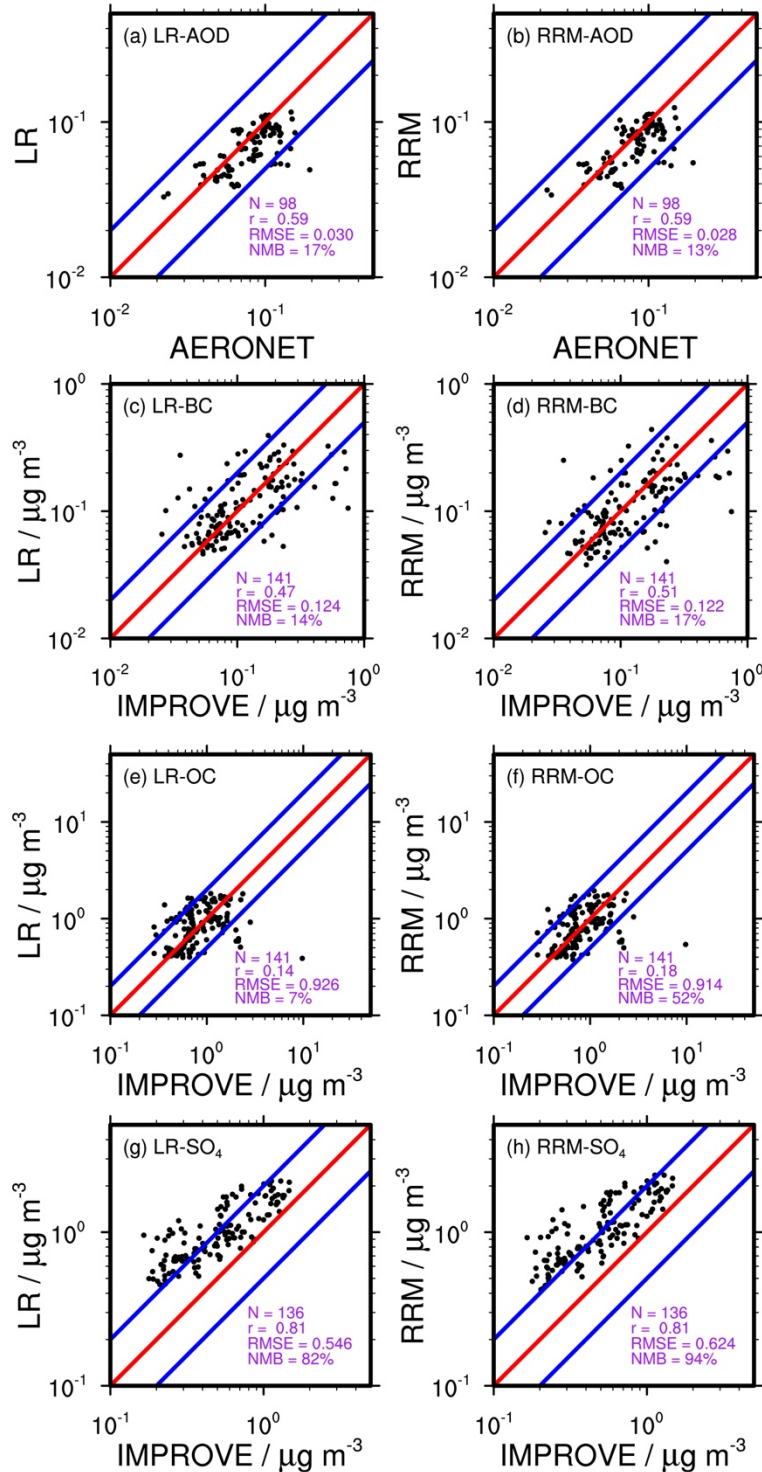
34 Figure S2. Evaluations of the (left column) LR and (right column) RRM simulated annual mean (a, b)
35 AOD at 550 nm and fine (c, d) BC, (e, f) organic carbon (OC), and (g, h) SO_4 mass concentrations against
36 ground-based observations from AERONET (AErosol RObotic NETwork) and IMPROVE (Interagency
37 Monitoring of Protected Visual Environments) (Malm et al., 1994) in the RRM region in 2016.
38 AERONET V3 level 2.0 provides daily mean AOD at 500 nm and daily mean Angstrom exponent for
39 440-870 nm (Slutsker, 2018), which are used to derive daily mean AOD at 550 nm. IMPROVE provides
40 daily mean mass concentrations of fine BC, OC, and SO_4 (Cira/Csu, 2023). The daily mean observations

41   are used to calculate monthly means, which are then used to select coincident model monthly results.
42   Notably, we use the regridded (1°× 1°) LR and RRM simulation results to match observational sites to
43   make the comparisons fair to both simulations. Each dot in the figure denotes one observational site. "N"
44   refers to the number of observational sites; "r" is the Pearson correlation coefficient; "RMSE" is the root
45   mean square error; and "NMB" indicates the normalized mean bias.
46   We apply the following equations to calculate the model fine BC, OC, and SO_4 to be compared with
47   observations.
48   SO_4(fine) = SO_4(accumulation mode) + SO_4(Aitken mode) + Sea salt(accumulation) + Sea salt(Aitken)
49   OC(fine) = (POM(primary carbon) + POM(accumulation) + SOA(accumulation) + SOA(Aitken))/1.4
50   BC(fine) = BC(accumulation) + BC(primary carbon)
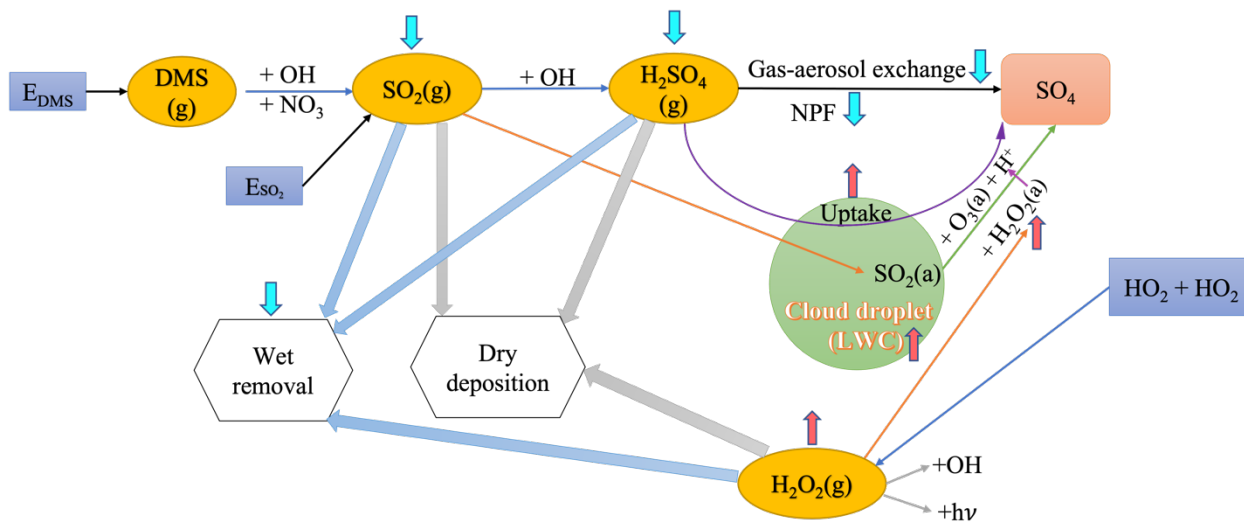
53   Figure S3~~1~~. Schematic of the impact of RRM on sulfur chemistry. Red upward arrows indicate
54   enhancement by RRM, while cyan downward arrows denote reduction by RRM.
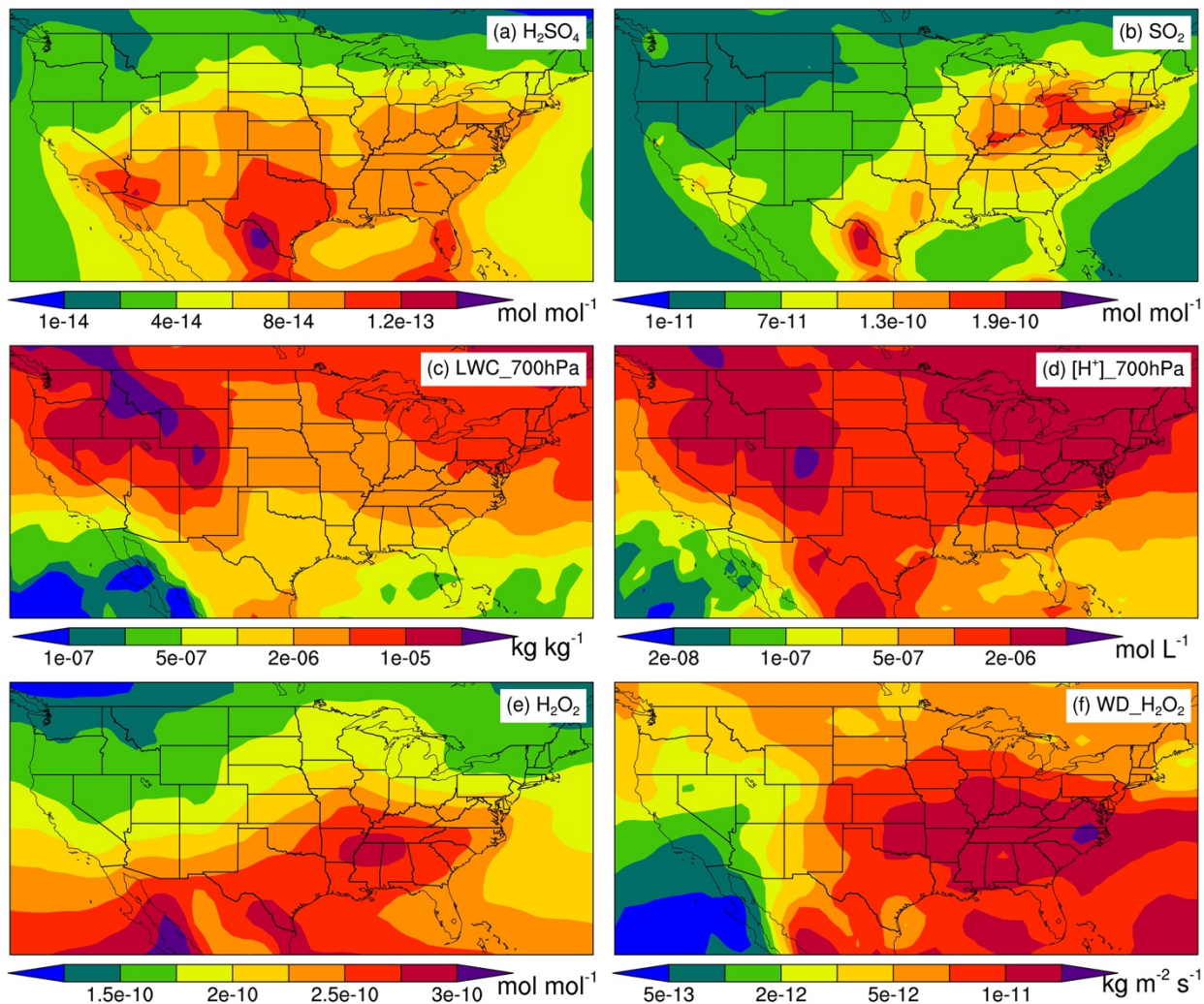
57 Figure S42. Spatial distributions of the annual mean (a) vertical-integrated gas-phase H_2SO_4
58 concentrations, (b) vertical-integrated gas-phase SO_2 concentrations, (c) large-scale cloud liquid water
59 content at 700 hPa (kg_{water} kg_{air}^{-1}), (d) H^+ concentrations in large-scale cloud liquid water at 700 hPa, (e)
60 vertical-integrated gas-phase H_2O_2 concentrations, and (f) wet deposition fluxes of gas-phase H_2O_2 from
61 the LR simulation.
62
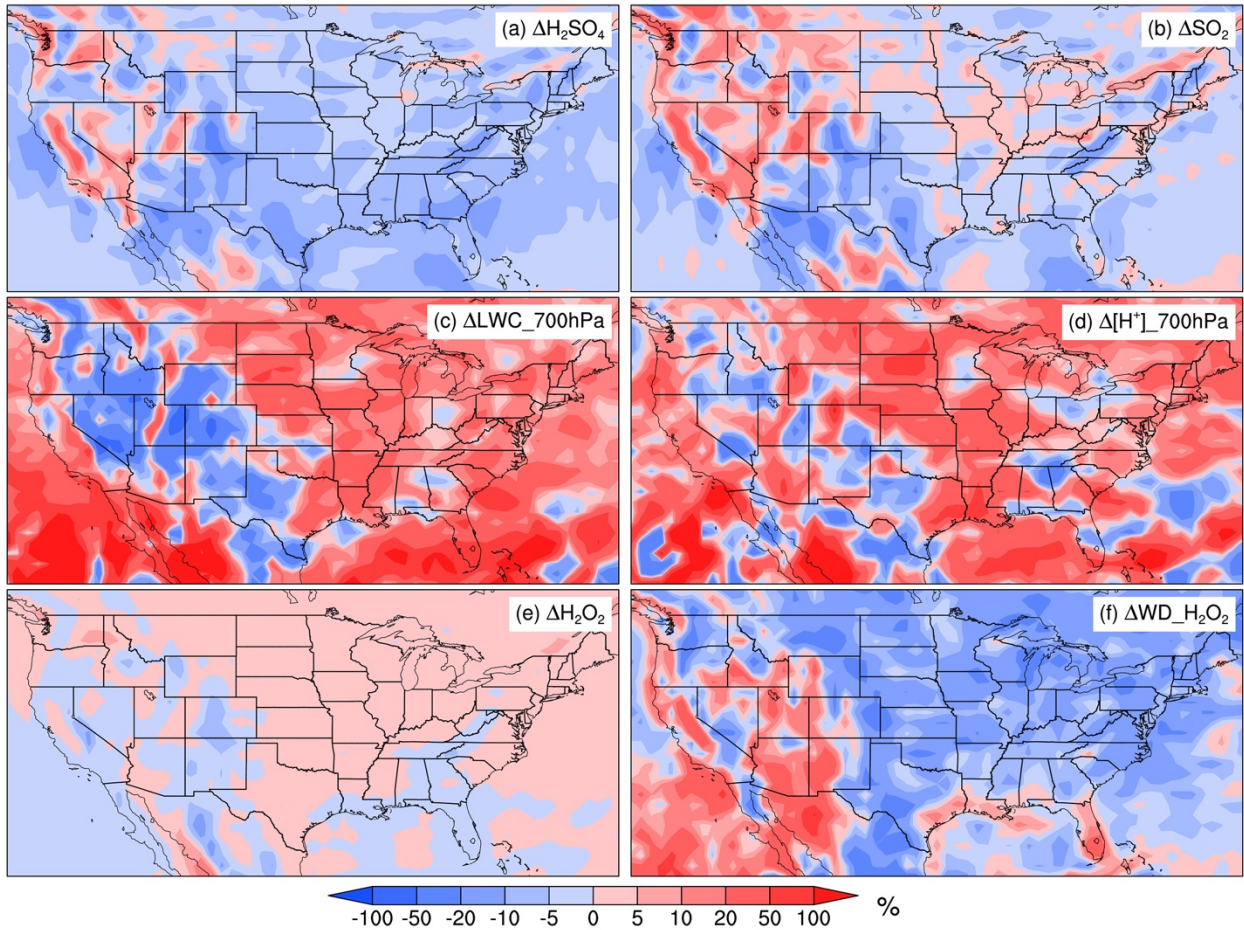
63
64   Figure S53. The same as Figure S2 but for the relative differences between the RRM and LR simulations.
65
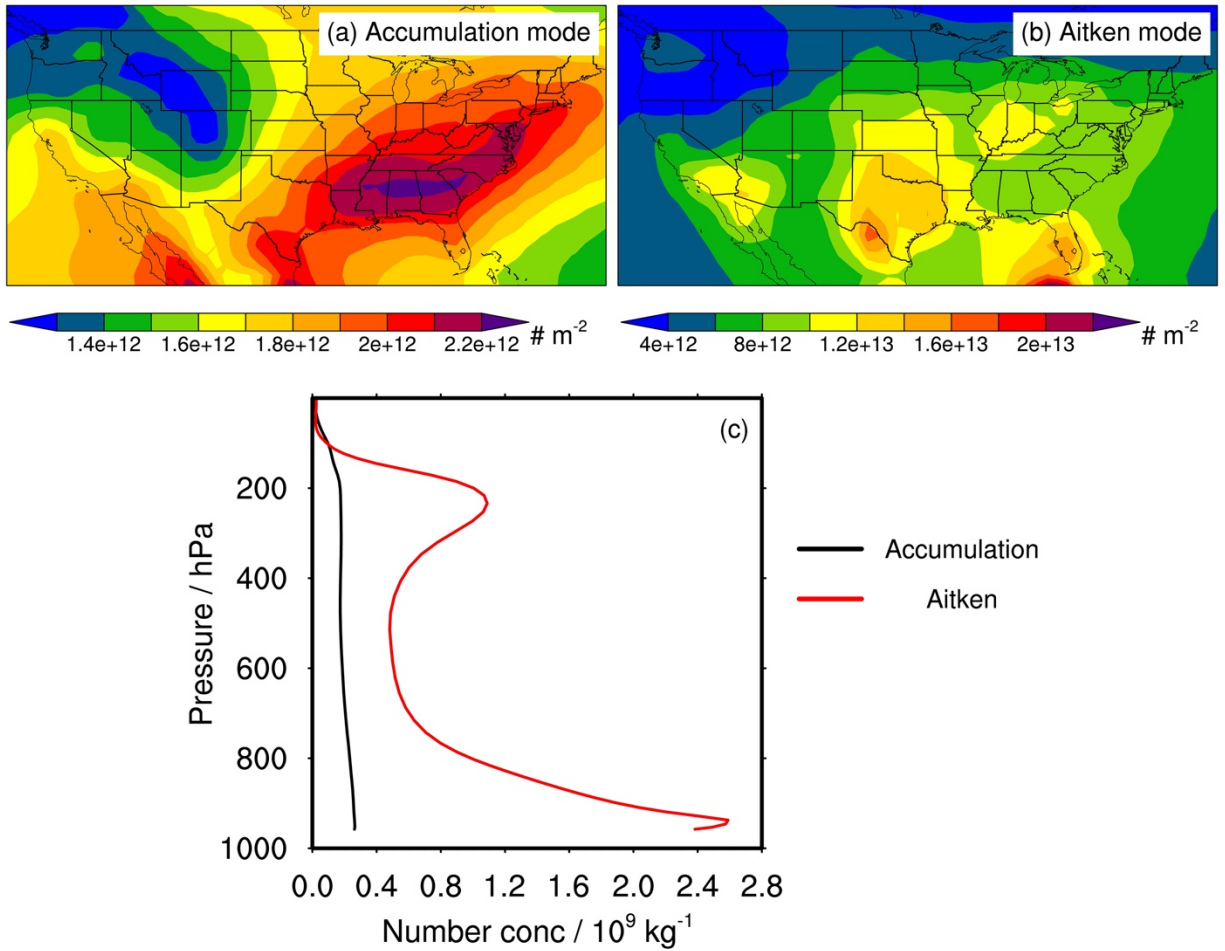
Figure S64. (a, b) Spatial distributions of annual mean vertical-integrated IAP number concentrations (# m^{-2}) for (a) accumulation and (b) Aitken modes from the LR simulation. (c) Vertical profiles of annual regional mean IAP number concentrations (10^9 kg$_{air}$$^{-1}$) for accumulation and Aitken modes from the LR simulation.
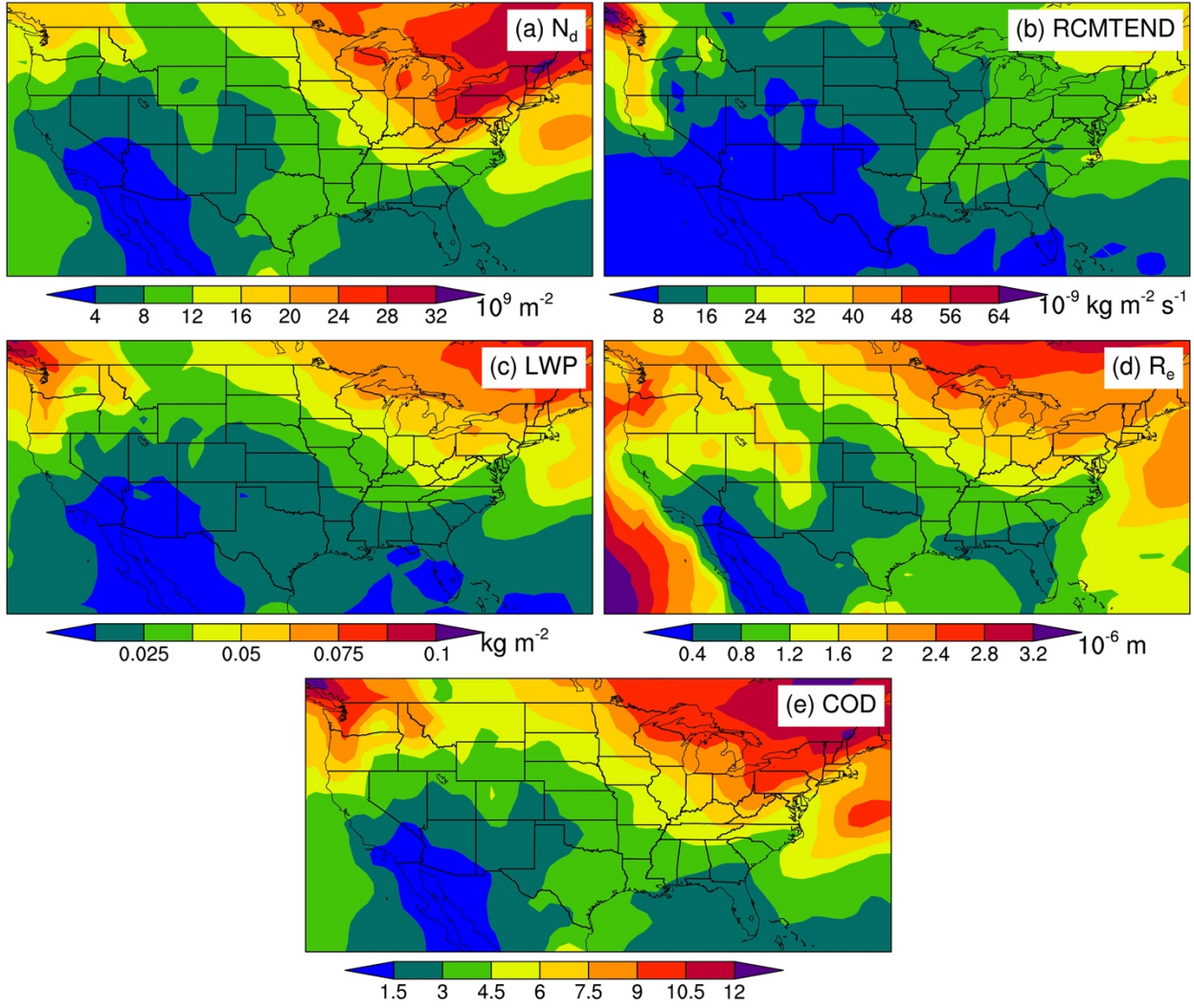
72
73   Figure S75. Same as Figure 12 but for the LR simulation results.
74
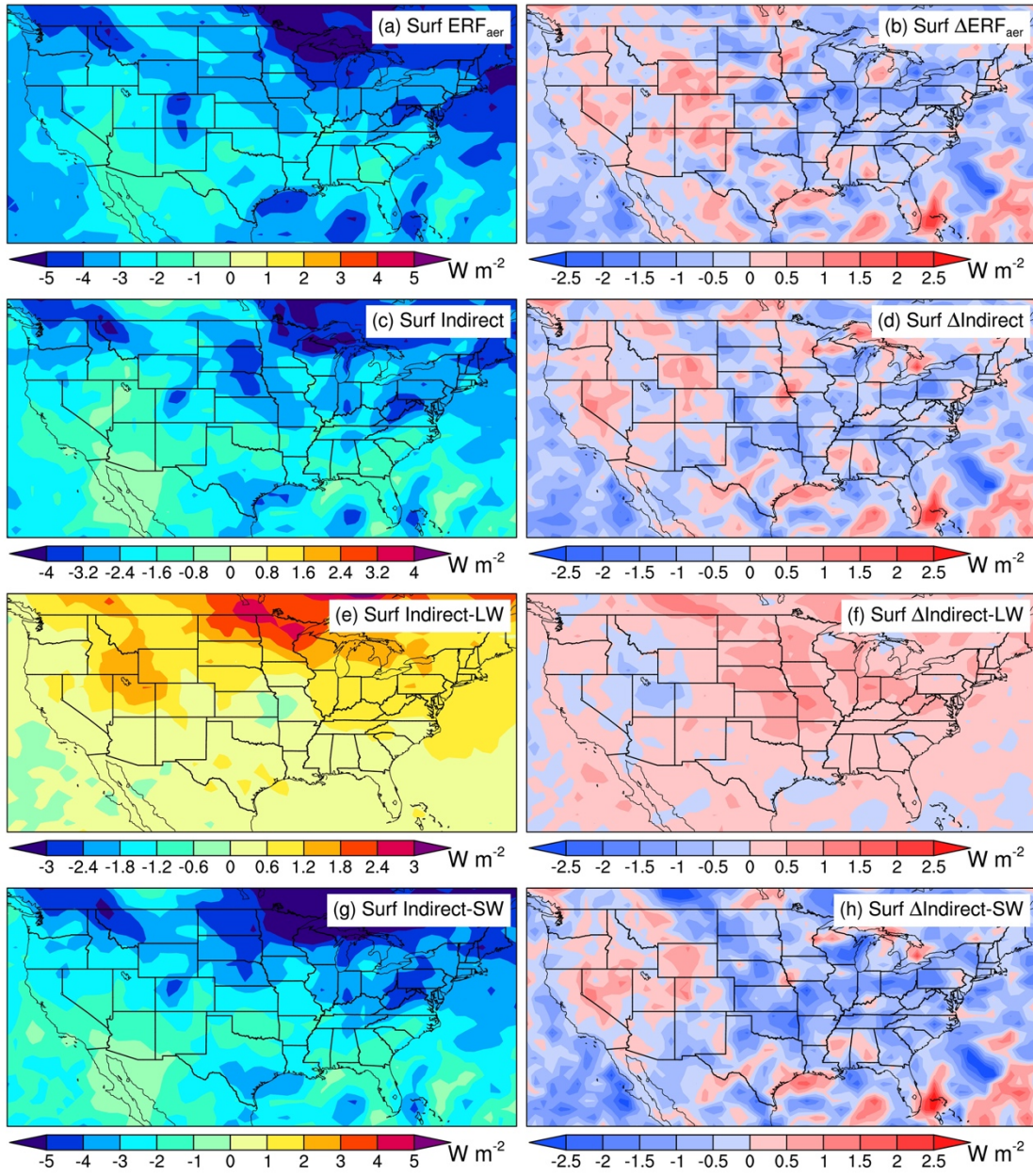
75
76   Figure S86. Same as Figure 13 but for surface ERF$_{aer}$.
77

References

CIRA/CSU: IMPROVE Data, Federal Land Manager Environmental Database [dataset], https://views.cira.colostate.edu/fed/QueryWizard/, 2023 (last access: May 26, 2022).

Malm, W. C., Sisler, J. F., Huffman, D., Eldred, R. A., and Cahill, T. A.: Spatial and seasonal trends in particle concentration and optical extinction in the United States, Journal of Geophysical Research: Atmospheres, 99, 1347-1370, https://doi.org/10.1029/93JD02916, 1994.

Platnick, S., King, M., and Hubanks, P.: MODIS Atmosphere L3 Monthly Product, NASA MODIS Adaptive Processing System, Goddard Space Flight Center [dataset], https://doi.org/10.5067/MODIS/MOD08_M3.061 (MOD08_M3) and https://doi.org/10.5067/MODIS/MYD08_M3.061 (MYD08_M3), 2015 (last access: Nov 28, 2023).

Slutsker, I.: Aerosol Robotic Network, Goddard Space Flight Center [dataset], https://aeronet.gsfc.nasa.gov/new_web/download_all_v3_aod.html, 2018 (last access: May 26, 2022).